

## Models for Stratiform Instability and Convectively Coupled Waves

ANDREW J. MAJDA

*Courant Institute of Mathematical Sciences, and Center for Atmosphere–Ocean Science, New York University, New York, New York*

MICHAEL G. SHEFTER

*Courant Institute of Mathematical Sciences, New York University, New York, New York*

(Manuscript received 28 February 2000, in final form 27 October 2000)

### ABSTRACT

A simplified intermediate model for analyzing and parameterizing convectively coupled tropical waves is introduced here. This model has two baroclinic modes of vertical structure: a direct heating mode and a stratiform mode. The key essential parameter in these models is the area fraction occupied by deep convection,  $\sigma_c$ . The unstable convectively coupled waves that emerge from perturbation of a radiative convective equilibrium are discussed in detail through linearized stability analysis. Without any mean flow, for an overall cooling rate of  $1 \text{ K day}^{-1}$  as the area fraction parameter increases from  $\sigma_c = 0.0010$  to  $\sigma_c = 0.0014$  the waves pass from a regime with stable moist convective damping to a regime of “stratiform” instability with convectively coupled waves propagating at speeds of roughly  $15 \text{ m s}^{-1}$ ; instabilities for a band of wavelengths in the supercluster regime,  $O(1000)$ – $O(2000)$  km; and a vertical structure with a “wave tilt” where the temperature structure in the upper troposphere lags behind that in the lower troposphere. Thus, these convectively coupled waves in the model reproduce several key features of convectively coupled waves in the troposphere processed from recent observational data by Wheeler and Kiladis. As the parameter  $\sigma_c$  is increased further to values such as  $\sigma_c = 0.01$ , the band of unstable waves increases and spreads toward a mesoscale wavelength of  $O(100)$  km while the same wave structure and quantitative features mentioned above are retained for  $O(1000)$  km.

A detailed analysis of the temporal development of instability of these convectively coupled waves is presented here. In the first stage of instability, a high convective available potential energy (CAPE) region generates deep convection and a front-to-rear ascending flow with enhanced vertical shear in a stratiform wake region. Thus, these intermediate models may be useful prototypes for studying the parameterization of upscale convective momentum transport due to organized convection. In the second stage of instability, detailed analysis of the CAPE budget establishes that the effects of the second baroclinic mode in the stratiform wake produce new CAPE, which regenerates the first half of the wave cycle. Finally, since these convectively coupled stratiform waves do not require a barotropic mean flow, a barotropic mean flow, which alters the surface fluxes, is added to study its effect on their stability. These effects of a barotropic mean flow are secondary; an easterly mean flow enhances instability of the eastward-propagating convectively coupled waves and diminishes the instability of the westward-propagating waves through a wind-induced surface heat exchange mechanism.

### 1. Introduction

Recent processing of observational data for convectively coupled equatorial waves in the troposphere (Wheeler and Kiladis 1999; Wheeler et al. 2000 and references therein) provides an interesting and important challenge for both wave theories to explain these structures and also for the capability of convective parameterization schemes to resolve these structures in general circulation models (GCMs). These remarkable eastward-propagating “Kelvin-like” waves have several robust features including a phase velocity of roughly  $15$

$\text{m s}^{-1}$  (Fig. 4 of Wheeler et al. 2000), a spatial extent in the lower troposphere on the order of  $1000$ – $2000$  km (G. N. Kiladis 1999, personal communication), and a vertical “wave tilt” with the upper-troposphere temperature structure lagging behind the lower-troposphere temperature structure. Since such waves extend into the lower stratosphere, there is recent speculation (Wheeler et al. 2000) that these convectively coupled waves might supply significant forcing for the quasi-biennial oscillation in the middle atmosphere. Another serious deficiency in GCM modeling concerns the erroneous representation of upscale convective momentum transport from organized mesoscale convective systems such as squall line clusters (Moncrieff and Klinker 1997).

A natural theoretical route for studying convectively coupled tropical waves and their parameterization is through intermediate models with cruder vertical res-

---

*Corresponding author address:* Prof. Andrew J. Majda, Courant Institute of Mathematical Sciences, New York University, 251 Mercer Street, New York, NY 10012.  
E-mail: jonjon@cims.nyu.edu

olution. Most of these studies have focused on models with a crude vertical resolution involving only a single dominant baroclinic heating mode coupled to deep convection (Emanuel 1987; Yano and Emanuel 1991; Neelin and Yu 1994; Yano et al. 1995, 1998; Majda and Shefter 2000). A notable exception is the interesting recent study of Mapes (2000) where an intermediate model is introduced with two layers of vertical resolution consisting of two baroclinic modes—a dominant heating mode and a stratiform mode—to allow for the effects of stratiform precipitation on convection (Houze 1997). The convective parameterization scheme utilized by Mapes in his intermediate model involves complicated parameterization of convective inhibition and subgrid-scale triggering energy besides stratiform mode coupling; numerical simulations of this intermediate model reveal convectively coupled waves emerging in some regions of parameters with qualitative features like those waves in the observations (Wheeler and Kiladis 1999; Wheeler et al. 2000).

In this paper, the authors introduce a simplified intermediate model for analyzing and parameterizing convectively coupled tropical waves with two baroclinic modes of vertical structure; a direct heating mode and a stratiform mode. This intermediate model, presented in detail in section 2, is a much simpler parameterization scheme than Mapes's model, conceptually, with fewer adjustable parameters, and does not utilize convective inhibition or subgrid-scale triggering energy. The essential parameters in the mass flux parameterization scheme introduced in section 2 are the area fraction occupied by deep convection  $\sigma_c$ , the subfraction  $\mu$  of the mass flux contributed to downdrafts from stratiform precipitation resulting from deep convection as compared with the mass flux contributed to downdrafts from deep convection, and the overall precipitation efficiency  $\Lambda$ ; furthermore, in an idealized limit where the stratiform heating mode is suppressed, a conceptually attractive parameterization of one-layer models involving instantaneous convective available potential energy (CAPE) adjustment (ICAPE) (Majda and Shefter 2000) emerges from this parameterization. The main results in this paper are presented in sections 3 and 4 and involve a detailed analysis of the unstable convectively coupled waves that emerge from linear theory around a radiative convective equilibrium (RCE). The time-dependent development of the unstable convectively coupled waves is studied in section 4. The convectively coupled waves arising from stratiform instability discussed in sections 3 and 4 occur with a vanishing mean wind and do not require a nontrivial barotropic mean flow. This contrasts strongly with the stable moist convective damping that occurs in simpler one-layer intermediate models with a vanishing barotropic mean wind (Emanuel 1987; Neelin and Yu 1994; Majda and Shefter 2000), where a nonzero barotropic mean is utilized to destabilize waves through wind-induced surface heat exchange (WISHE). In section 5 the effect of a baro-

tropic mean wind on the convectively coupled waves generated through stratiform instability is studied. In general the WISHE instability is a secondary effect; for an easterly mean wind, in general the instability of the eastward convectively coupled stratiform wave is enhanced while the instability of the westward wave is diminished or even completely suppressed.

## 2. A model parameterization with stratiform modes

Most of the intermediate models used for short-term climate prediction in the Tropics involve very crude resolution in the vertical direction (Neelin and Zeng 2000, hereafter NZ00). A number of recent studies utilize various implementations of models with one vertical baroclinic mode (OVBM) (Yano et al. 1995, 1998, and references therein; NZ00; Majda and Shefter 2000), with or without a barotropic mean wind. The OVBM models can reproduce some variability of tropical waves and predict their speeds of propagation with a reasonable accuracy. However, wave structures generated by the OVBM models cannot represent correctly many important phenomena observed in the Tropics. For example, convective momentum transport in tropical squall lines (Moncrieff 1992; Emanuel 1994) is accompanied by such elements as ascending front-to-rear flows with enhanced vertical shear and descending return flows that clearly require better vertical resolution.

The model with two vertical baroclinic modes (TVBM), developed in this section, is a natural generalization of the OVBM models, which can reproduce tropical waves with a more complicated vertical structure. The large-scale dynamics is based on two dynamically active baroclinic modes of the primitive equations and a passive mean barotropic component. Conceptually, the large-scale dynamical model is similar to the stratiform wave model of Mapes (2000), which was designed primarily for direct numerical simulations. However, in the model developed here, many complicated details of Mapes's formulation are deliberately avoided. In particular, one of the goals of this study is to present quantitative analytical evidence that the same regimes of instability occur in the simplest parameterized models with stratiform instability.

The thermodynamic model includes the middle troposphere that communicates with the subcloud boundary layer at the bottom through latent heat exchanges and downdrafts and also has energy loss through radiation at the top. Small-scale convection is parameterized through the ICAPE adjustment scheme introduced by Majda and Shefter (2000). All dynamic and thermodynamic variables in the TVBM model are projected on the first and second baroclinic modes, in a way consistent with the physical context. The detailed derivation of prognostic equations is given below in section 2a. The connection between the OVBM and TVBM models

is made explicit in section 2b by shutting off the second baroclinic mode effects. Finally, typical radiative convective equilibria that arise in the TVBM model are summarized in section 2c.

### a. Derivation of the dynamical equations

Basic prognostic and diagnostic equations of the TVBM model are derived in this subsection by projecting the full three-dimensional equations on the first and second baroclinic modes. All forcing and source terms in these equations are represented by projections on the two baroclinic modes, according to the physical context.

#### 1) DYNAMICS OF LARGE-SCALE VARIABLES

The dynamic core of the model is based on the Bousinesq equations in  $z$  coordinates (Pedlosky 1979),

$$\begin{aligned} \frac{D\mathbf{v}}{Dt} &= -\nabla_H p - C_D(\mathbf{v}_H)\mathbf{v} - \tau_D^{-1}\mathbf{v}, \\ u_x + v_y + w_z &= 0, \\ \frac{D\theta}{Dt} + \alpha w &= S, \quad \tilde{H}\frac{\partial p}{\partial z} = \bar{\alpha}\theta, \end{aligned} \quad (2.1)$$

where  $\mathbf{v} = [u(x, y, z, t), v(x, y, z, t)]$  is the horizontal velocity field,  $w(x, y, z, t)$  is the vertical velocity,  $\theta(x, y, z, t)$  is the potential temperature, and  $p$  is the pressure. The constant  $\alpha$  is given by  $\alpha = (N^2\theta_0)/g$ , with  $\theta_0 = 300$  K, the temperature above the boundary layer. The hydrostatic balance equation in (2.1) is the  $z$  coordinate transform of the formula in (9) of Emanuel (1987) for baroclinic disturbances so that  $\bar{\alpha} = c_p\gamma\epsilon$ , where  $\epsilon$  measures the magnitude of the variations of potential temperature through the troposphere above the boundary layer,  $\epsilon = (\theta_0 - \bar{\theta})/\theta_0 \approx 0.1$ . The height  $\tilde{H}$  is a specific constant proportional to the height of the troposphere,  $H_T$ , and will be specified later. See Table 1 for the remaining constants in (2.1).

The momentum drag and Rayleigh friction are represented by terms  $C_D(\mathbf{v}_H)\mathbf{v}$  and  $\tau_D^{-1}\mathbf{v}$  in (2.1), respectively. The source term  $S$  represents feedbacks from convective heating and radiative cooling to the large-scale dynamics. Note that the derivative operator,  $\bar{D}/Dt = \partial/\partial t + \bar{u}\partial/\partial x$ , includes only advection by the barotropic mean flow but does not have nonlinear advection terms. Since this paper is focused on linearized stability analysis near radiative-convective equilibria that carry no large-scale flow, it is reasonable to omit the nonlinear advective terms in (2.1). Furthermore, for the linearized analysis in sections 3, 4, and 5 below, the standard Galilean transformation is utilized to reduce the substantial derivative operator,  $\bar{D}/Dt$ , to the temporal partial derivative,  $\partial/\partial t$ . As usual, rigid-lid boundary conditions are assumed to be valid both at the top and at the bottom of the troposphere with height  $H_T$ . The effects of ro-

TABLE 1. Model parameters.

$C_w^0 = 1.2 \times 10^{-3}$ , surface-flux rate by wind
$C_D^0 = 10^{-3}$ , surface heating coefficient
$u_0 = 5$ m s $^{-1}$ , size of turbulent velocity fluctuations in the boundary layer
$N^2 = 10^{-4}$ s $^{-2}$ , Brunt-Väisälä buoyancy frequency
$\epsilon = (\theta_0 - \bar{\theta})/(\theta_0) \approx 0.1$ , strength of temperature fluctuations in the troposphere
$\theta_0 = 300$ K; temperature at the top of the boundary layer
$\theta_{cb}^*$ = 10 K; size of fluctuations in the boundary layer moist potential temperature
$\bar{\theta}_{cb} - \bar{\theta}_{em} = 20$ K; boundary layer and middle troposphere potential temperature discrepancy at RCE
$\Lambda = 0.9$ , precipitation efficiency coefficient
$\Gamma_m = 6 \times 10^{-3}$ K m $^{-1}$ , moist lapse rate
$\gamma = 1.7$ , ratio of moist and dry lapse rates
$c_p = 10^3$ J K $^{-1}$ kg $^{-1}$ , specific heat at constant pressure
$Q_{r0} = -1$ K day $^{-1}$ , mean radiative cooling rate
$\tau_R = 50$ days, longwave radiation relaxation time
$\tau_D = 75$ days, Rayleigh-forcing timescale
$\tau_S = 0.25$ , stratiform heating fraction
$H = 8$ km, average height of penetrative convection
$H_m = 5$ km, depth of the middle-level troposphere (a level of minimum moist potential temperature)
$h = 500$ m, thickness of subcloud boundary layer
$\mu = 0.5$ , relative strength of stratiform convection downdrafts
$b = 0.9$ , weight of second baroclinic horizontal velocity contribution to the boundary layer drag
$\alpha_2 = 0.1$ , weight of second baroclinic potential temperature contribution to CAPE
$H_T = 10$ km, height of troposphere, $\bar{H} = H_T/\pi$
$\bar{H} = \bar{H}^2/H_m$ , scale height in (2.1)
$\bar{\lambda} = \bar{H}/H$ , scale factor for (2.2)

tation and large-scale meridional motion will not be considered in this paper and will be discussed elsewhere.

In the TVBM model the vertical structure contains two baroclinic modes, with corresponding basis functions,  $G_1(z)$  and  $G_2(z)$ , so that

$$\begin{aligned} \begin{pmatrix} \mathbf{v} \\ p \end{pmatrix} &= \begin{pmatrix} \mathbf{v}_1 \\ p_1 \end{pmatrix} G_1(z) + \begin{pmatrix} \mathbf{v}_2 \\ p_2 \end{pmatrix} G_2(z), \\ \begin{pmatrix} w \\ \theta \\ S \end{pmatrix} &= \begin{pmatrix} w_1 \\ \theta_1 \\ S_1 \end{pmatrix} \bar{\lambda} \bar{H} (-G_1') + \begin{pmatrix} w_2 \\ \theta_2 \\ S_2 \end{pmatrix} \bar{\lambda} \bar{H} (-G_2'), \end{aligned} \quad (2.2)$$

where  $G' = dG/dz$ . The explicit basis functions for the first and second baroclinic modes are normalized in the following way:

$$G_1(z) = \cos\left(\frac{z}{\bar{H}}\right), \quad G_2(z) = -\cos\left(\frac{2z}{\bar{H}}\right), \quad (2.3)$$

where  $\bar{H} = H_T/\pi$  and  $\bar{\lambda}$  is a convenient dimensionless order one constant chosen below. This choice of the basis functions leads to a physically meaningful representation of the flow and heating patterns associated with deep and stratiform convection (Houze 1997). For example, flows with a positive projection on the first baroclinic mode and a zero projection on the second baroclinic mode correspond to the deep penetrative convection events, with a typical positive shear profile of

the horizontal velocity and strong convective heating in the middle of the troposphere. On the other hand, an addition of a small positive component of the second baroclinic mode to these profiles modifies zonal velocities by enhancing the shear in the upper troposphere and reducing it in the lower troposphere. Cooling anomalies of the lower troposphere and warming anomalies of the upper troposphere produced by the second baroclinic component of convective heating, contribute to the formation of typical “top-heavy” heating profiles that are often observed in the regions of stratiform convection (Mapes and Houze 1995).

The scaling constant  $\bar{\lambda}$  in (2.2) does not affect the wave speed of the corresponding shallow water equation. After eliminating  $w$  via the conservation of mass with the choice of  $\bar{\lambda} = \tilde{H}/\bar{H}$ , the projected dynamic equations in (2.1) transform to

$$\begin{aligned} \frac{\partial \mathbf{v}_{H,j}}{\partial t} - \bar{\alpha} \nabla_H \theta_j &= -C_{D,j}(\mathbf{v})\mathbf{v}_j - (\tau_D)^{-1}\mathbf{v}_j, \\ \frac{\partial \theta_j}{\partial t} - \bar{\alpha} \xi_j \operatorname{div}_H \mathbf{v}_j &= S_j, \quad j = 1, 2. \end{aligned} \quad (2.4)$$

Here, the coefficients  $\xi_1 = 1$  and  $\xi_2 = 1/4$  correspond to the first and second baroclinic modes (Matsuno 1966; Gill 1982). The product  $\bar{\alpha} \bar{\alpha}$  is the square of the wave speed of the first baroclinic mode for the dry gravity waves, which is set at  $50 \text{ m s}^{-1}$ ; this requirement is satisfied provided  $\bar{H}^2/\tilde{H} = 5 \text{ km}$ . With the explicit form of the first baroclinic mode in (2.2), (2.3) in the model, this sets the middle of the troposphere at  $H_m = 5 \text{ km}$  so that the height of the troposphere is given by  $H_T = 10 \text{ km}$ . The coefficient  $\bar{\alpha}$  is given by  $\bar{\alpha} = H_m \alpha = H_m(N^2\theta_0)/g$ . The coefficients  $\bar{\alpha}$ ,  $\bar{\alpha}$  are the same ones that enter in the OVBM models (Yano and Emanuel 1991; Yano et al. 1995; Majda and Shefter 2000) and are convenient choices for comparison of phenomena in the TVBM models with that already documented in the OVBM models.

The speeds of the dry gravity waves, 50 and 25  $\text{m s}^{-1}$  in the model, compare quite well with the two dominant spectral peaks calculated by Mapes and Houze (1995) from observed data at 52 and 23  $\text{m s}^{-1}$ . The explicit analytic form for the vertical profile structure in (2.3) in  $z$  coordinates is useful for clarifying and interpreting the arguments in subsequent sections of the paper. The equations in (2.4) describe the large-scale dynamics in the TVBM model via two damped and driven shallow-water equations. In the following, the TVBM equations for thermodynamic effects are developed utilizing the same projection methodology.

## 2) HEATING AND COOLING EFFECTS

The source terms,  $S_1$  and  $S_2$ , in (2.4) describe both the effects of convective heating,  $q_1$ ,  $q_2$ , and radiative cooling,  $Q_{R1}$ ,  $Q_{R2}$ , partitioned into two baroclinic components,

$$S_1 = q_1 + Q_{R1}, \quad S_2 = q_2 + Q_{R2}. \quad (2.5)$$

The first baroclinic component of convective heating,  $q_1$ , is associated with small-scale vertical gusts of deep penetrative convection and is parameterized through the ICAPE convective parameterization (Majda and Shefter 2000). In the ICAPE parameterization, in the regions of deep convection, the contributions in the vertical momentum equation from the vertical velocity are assumed to be balanced instantaneously by the buoyancy,  $B$ ,

$$H^{-1} \frac{w_c^2}{2} \approx \frac{\partial \left( \frac{1}{2} w_c^2 \right)}{\partial z} = B \approx \frac{c_p \Gamma_m}{\theta_0} (\theta_{eb} - \gamma \theta),$$

with  $\Gamma_m$  the moist lapse rate, so that  $\text{CAPE} = 2HB = 2Hc_p\Gamma_m(\theta_{eb} - \gamma\theta)/\theta_0$ . Also, the deep penetrative events are assumed to have a uniform velocity,  $w_c$ , through a height  $H$ , which is set at  $H = 8 \text{ km}$  (Yano et al. 1995), and occur throughout an area fraction  $\sigma_c$  of the region. The CAPE is proportional to the difference between the moist equivalent potential temperature in the boundary,  $\theta_{eb}$ , and the saturated value of moist equivalent potential temperature in the lower middle troposphere,  $\theta_{em}^*$ , which is approximated by  $\gamma\theta$  [for more details, see Yano et al. (1995) and Majda and Shefter (2000)].

With these approximations, the ICAPE parameterization is given by

$$q_1 = a_0(\text{CAPE})^{1/2} = a_0 w_c, \quad a_0 = \frac{\bar{\alpha} \sigma_c}{H_m}. \quad (2.6)$$

With the basis functions defined in (2.3),  $\bar{H}(-G'_1) \approx 1$  near the middle of the troposphere, while  $\bar{H}(-G'_2)$  is a small number whose magnitude and sign depend on the CAPE sampling location,  $z_{\text{limt}}$ . Therefore,  $\theta_{\text{limt}}$  can be expressed approximately through the first and second baroclinic projections,  $\theta_1$  and  $\theta_2$  as follows:

$$\begin{aligned} \theta_{\text{limt}} &= \bar{H} \{ [-G'_1(z_{\text{limt}})]\theta_1 + [-G'_2(z_{\text{limt}})]\theta_2 \} \\ &\approx \theta_1 - \alpha_2 \theta_2, \quad \alpha_2 = 2G'_2(z_{\text{limt}}). \end{aligned} \quad (2.7)$$

The parameter  $\alpha_2$  is typically positive and small in the lower middle troposphere because  $G'_2$  is positive in that vertical region from (2.3); the value  $\alpha_2 = 0.1$  will be utilized in concrete applications throughout the rest of this paper. With the notation introduced above, CAPE and the intensity of convective updrafts,  $w_c$ , can be computed approximately as follows,

$$\text{CAPE} = 2H \frac{c_p \Gamma_m}{\theta_0} (\theta_{eb} - \gamma\theta_1 + \alpha_2 \gamma\theta_2),$$

$$w_c = \begin{cases} (\text{CAPE})^{1/2}, & \text{CAPE} > 0 \\ 0, & \text{otherwise.} \end{cases} \quad (2.8)$$

Note that second baroclinic mode warming anomalies,  $\theta_2 > 0$ , tend to enhance CAPE, in contrast to first baroclinic mode warming anomalies that reduce CAPE, according to (2.8).

To describe the dynamics of the stratiform heating intensity,  $q_2$ , the authors follow the “delayed” adjustment model introduced by Mapes (2000),

$$\frac{\partial q_2}{\partial t} = \frac{1}{\tau_s}(sq_1 - q_2), \quad (2.9)$$

where  $\tau_s$  is the stratiform adjustment time, and  $s$  is the fraction of the direct heating mode to which  $q_2$  tends to adjust.

According to (2.2), the relative strengths of the two baroclinic components of radiative cooling,  $Q_{R1}$ ,  $Q_{R2}$ , must be weighted with respect to  $(-G'_1)$  and  $(-G'_2)$  calculated at a location near the top of the troposphere,  $z = H_{\text{top}}$  where radiative cooling is maximized. Since both  $(-G'_1)$  and  $(-G'_2)$  are positive at  $H_{\text{top}}$ , their ratio is also positive. This ratio determines how the total radiative cooling rate,  $Q_{R0} - \theta/\tau_R$ , is distributed between the first and second baroclinic modes,

$$\begin{aligned} Q_{R1} &= \frac{1}{1+s}Q_{R0} - \frac{1}{1+s}\frac{\theta_1}{\tau_R}, \\ Q_{R2} &= \frac{s}{1+s}Q_{R0} - \frac{s}{1+s}\frac{\theta_2}{\tau_R}, \end{aligned} \quad (2.10)$$

where  $1/(1+s)$  and  $s/(1+s)$  represent the relative magnitudes of  $(-G'_1)$  and  $(-G'_2)$  at  $z = H_{\text{top}}$ . Note that the same constant  $s$  is utilized here as in (2.9) in order to guarantee a balance between heating and cooling at radiative convective equilibrium (RCE).

### 3) BOUNDARY LAYER DYNAMICS AND DOWNDRAFTS

The dynamics of the boundary layer equivalent potential temperature,  $\theta_{eb}$ , is governed by the downdrafts,  $D$ , and latent heat from the ocean surface,  $E$  (Yano et al. 1995, 1998),

$$h\frac{\partial \theta_{eb}}{\partial t} = -D + E, \quad E = C_\theta(\mathbf{v})(\theta_{eb}^* - \theta_{eb}),$$

$$D = -[(1 - \sigma_c)w_e^\downarrow - \sigma_c w_d](\theta_{eb} - \theta_{em}). \quad (2.11)$$

In this equation,  $\theta_{eb}^*$  is the saturated moist equivalent potential temperature in the boundary layer,  $w_e^\downarrow$  represents the environment downdrafts, activated only when  $w_e < 0$ , and  $w_d$  is the convective downdraft term so that  $m = \sigma_c w_d$  is the mass flux due to convective downdrafts. The somewhat peculiar notation with the downward mass flux,  $m = \sigma_c w_d$  and also in (2.11) for  $-D$ , is utilized throughout this section both for simple comparison of the TVBM and OVBM models and as an aid for readers familiar with OVBM models. Both  $w_e$  and  $w_d$  enter (2.11) in the same way as in the OVBM models; however, they need to be generalized for the TVBM model. The environmental downdrafts are evaluated using the middle lower-troposphere values and are distributed between the two baroclinic modes with the weights calculated in (2.7),

$$w_e \approx w_{e1} - \alpha_2 w_{e2}, \quad (2.12)$$

where the first baroclinic component of the environment downdrafts,  $w_{e1}$ , is defined exactly as in the OVBM model, through the incompressibility constraint with  $w_{e2}$  defined similarly,

$$\begin{aligned} w_{e1} &= -(\sigma_c w_c + H_m \text{div}_H \mathbf{v}_1), \\ w_{e2} &= -\left(\frac{H_m}{\alpha} q_2 + \frac{H_m}{4} \text{div}_H \mathbf{v}_2\right). \end{aligned} \quad (2.13)$$

Following Yano and Emanuel (1991), there is a mass flux upward of ascending air from the deep convection,  $m_+$ , and also downdrafts in the boundary layer with a mass flux,  $m = \sigma_c w_d$  from (2.11), which are assumed to arise from shallow updraft–downdraft couplets so that

$$\sigma_c w_d = m = \frac{1 - \Lambda}{\Lambda} m_+,$$

with  $\Lambda$ , the precipitation efficiency. The upward mass flux is assumed to split into a weighted sum of mass flux contributions from both the direct deep convection,  $m_c$ , and the stratiform heating regions,  $m_s$ , so that

$$\begin{aligned} m_+ &= (1 - \mu)m_c + \mu m_s, \quad m_c = \sigma_c w_c, \\ m_s &= \frac{H_m}{\alpha} q_2 s^{-1}. \end{aligned} \quad (2.14)$$

The stratiform region occurs over a much wider area with considerably weaker vertical motion (Mapes and Houze 1995), which is assumed here to contribute to the nontrivial contribution,  $\mu m_s$ , to the mass flux in (2.14).

Finally,  $\theta_{em}$  is typically associated with a neutral standing mode and does not influence other modes in any significant way (Emanuel 1994; Majda and Shefter 2000). For simplicity,  $\theta_{em}$  will be replaced by its RCE value of the one-and-a-half layer model,  $\theta_{em}$ , throughout the rest of the paper.

### 4) TURBULENT AND MOMENTUM DRAG

Boundary layer drag terms in (2.4) and (2.11) are parameterized according to the model proposed by Nee- lin and Zeng (2001),

$$\begin{aligned} C_D(\mathbf{v}) &= \frac{C_D^0}{h}[u_0^2 + (\bar{u} + \mathbf{v}_1 - b\mathbf{v}_2)^2]^{1/2}, \\ C_\theta(\mathbf{v}) &= \frac{C_\theta^0}{h}[u_0^2 + (\bar{u} + \mathbf{v}_1 - b\mathbf{v}_2)^2]^{1/2}, \end{aligned} \quad (2.15)$$

where  $h$  is the depth of the boundary layer,  $\bar{u}$  is the barotropic wind,  $u_0$  is the intensity of turbulent velocity fluctuations in the boundary layer, and  $C_D^0$  and  $C_\theta^0$  are surface drag coefficients. The constant  $b$  is determined in a way consistent with the projection procedure, using the decomposition of  $u$  at the top of the boundary layer,  $\mathbf{v}|_{z=h} = G_1(h)\mathbf{v}_1 + G_2(h)\mathbf{v}_2$ . Then, since  $G_1(h) > 0$  and

$G_2(h) < 0$  from (2.3), the ratio  $b = -G_2(h)/G_1(h)$  is positive, and it expresses the relative strength of the second baroclinic velocity component. The following formulas describe how momentum drag is distributed between the first and second baroclinic components,

$$C_{D,1} = \frac{1}{1+b} \frac{C_D^0}{h} [u_0^2 + (\bar{u} + \mathbf{v}_1 - b\mathbf{v}_2)^2]^{1/2},$$

$$C_{D,2} = \frac{b}{1+b} \frac{C_D^0}{h} [u_0^2 + (\bar{u} + \mathbf{v}_1 - b\mathbf{v}_2)^2]^{1/2}. \quad (2.16)$$

### 5) SUMMARY OF PROGNOSTIC AND DIAGNOSTIC EQUATIONS

In the TVBM model, basic equations are derived by projecting all appropriate variables on the first and second baroclinic modes in a self-consistent way. All prognostic and diagnostic variables are summarized below.

The first and second baroclinic components of the horizontal velocity and dry temperature are determined prognostically according to (2.4). The remaining prognostic variables include the stratiform convective heating component,  $q_2$ , determined by (2.9) and  $\theta_{eb}$ , described by (2.11).

Direct convective heating,  $q_1$ , and the small-scale vertical updrafts associated with it, are determined diagnostically according to (2.6), (2.8). Environmental and convective downdrafts are also determined diagnostically via (2.12), (2.13), (2.14).

#### b. Connection with OVBM model

Many features of the two-and-a-half layer model are inherited from the one-and-a-half layer model. The relationship between these models can be made quantitative if the stratiform mode feedbacks to one-layer dynamics are switched off,  $\alpha_2 = 0$ ,  $b = 0$ , and stratiform adjustment is assumed to occur instantaneously so that stratiform heating,  $q_2$ , becomes diagnostically linked to  $q_1$  through the right-hand side of (2.9) at equilibrium. It is easy to check that contributions from the stratiform mode to the boundary layer dynamics in (2.11) disappear, and this equation becomes equivalent to its OVBM counterpart uniformly for all values of  $\mu$ . In the limit,  $\tau_s \ll 1$ , the equations for  $\mathbf{v}_1$  and  $\theta_1$  in (2.4) are also equivalent to their analogs in the OVBM model, with only slightly different damping coefficients. Then, the stratiform mode is simply a slave mode of the one-layer dynamics and carries no extra variability.

If the effects of small-scale convective downdrafts are switched off in (2.11), that is,  $\sigma_c$  is set identically to zero formally, then with (2.12), (2.13), it follows that the downdrafts are determined completely by the large-scale environmental convergence. Thus, with these special assumptions, the model parameterization becomes a wave-CISK parameterization (Kuo 1974; Lindzen

1974; Emanuel 1994) with two vertical baroclinic modes. If the parameters  $\alpha_2$ ,  $b$  are set to zero, then the prognostic equations become a wave-CISK parameterization in a OVBM model with the stratiform mode as a slave variable. The linearized analysis in Majda and Shefter (2000) for the OVBM model yields the familiar ‘‘ultraviolet catastrophe’’ in wave-CISK parameterization.

#### c. Typical radiative convective equilibria

With the convective mass flux,  $m_c = \sigma_c w_c$ , the radiative equilibrium in the TVBM model has the form,

$$\frac{\bar{\alpha}}{H_m} \bar{m}_c + \frac{1}{1+s} Q_{R0} = 0,$$

$$C_\theta^0 (u_0^2 + \bar{u}^2)^{1/2} (\theta_{eb}^* - \bar{\theta}_{eb}) = \bar{m}_c \left( \frac{1}{\Lambda} - \alpha_2 s \right) (\bar{\theta}_{eb} - \bar{\theta}_{em}),$$

$$s \frac{\bar{\alpha}}{H_m} \bar{m}_c = \bar{q}_2, \quad \frac{\bar{m}_c}{\sigma_c} = \bar{w}_c,$$

$$\bar{w}_c = \left( \frac{c_p \Gamma_m}{\theta_0} \right)^{1/2} (2H)^{1/2} (\bar{\theta}_{eb} - \gamma \bar{\theta}_1 + \gamma \alpha_2 \bar{\theta}_2)^{1/2},$$

$$\bar{\theta}_1 + s \bar{\theta}_2 = 0. \quad (2.17)$$

The benchmark set of parameter values for the RCE used in this paper is listed in Table 1 and is essentially the same set as in Yano et al. (1995), Majda and Shefter (2000), except for minor changes. For these parameter values,  $\theta_{eb} - \bar{\theta}_{em} = 20$  K. The results of linear theory for another weaker RCE with  $\bar{\theta}_{eb} - \bar{\theta}_{em} = 5$  K will also be discussed briefly below. Note that the mass flux  $\bar{m}_c$  is uniquely specified from  $Q_{R0}$  in the first equations from (2.17) while the second and third equations yield  $\bar{\theta}_{eb}$ ,  $\bar{q}_2$  from the mass flux and other specified parameters. The RCE itself is independent of the parameters,  $\mu$ ,  $\tau_s$  in the model and has very weak dependence on  $\Lambda$  and  $\alpha_2$ . The sensitivity of linear theory at RCE to these parameters is described in section 3b below. On the other hand, for fixed external parameters in the RCE, the mass flux,  $\bar{m}_c$ , is determined so the strength of deep convective updrafts  $\bar{w}_c$  in RCE can be varied systematically by varying  $\sigma_c$ ; the changes in linear theory at RCE varying  $\sigma_c$  are studied in section 3. For an RCE with specified  $\bar{m}_c$ , one can also vary the height,  $H = \hat{H} H_0$  with  $H_0 = 8$  km together with  $\hat{\sigma}_c = \sigma_c \hat{H}^{-1/2}$  so that the mass flux,  $m_c$ , remains constant. However, in the nondimensional units utilized in the linear theory at RCE, this is completely equivalent to keeping  $H$  constant and varying  $\sigma_c$ . See the description below (3.1).

### 3. Waves and instabilities in the model parameterization

The system of prognostic and diagnostic equations for convectively coupled dynamics in the Tropics was

derived in the previous section. The linearized wave and stability analysis of these equations near radiative convective equilibria in the absence of mean barotropic wind are the subject of discussion in this section, with the emphasis on the instability of stratiform waves. The effects of a barotropic mean wind will be discussed later in section 5.

For the further discussion, it is convenient to switch to the nondimensional variables that can be formed by using the following scales: (a) the length scale,  $L =$

1500 km, the equatorial Rossby radius; (b) the velocity scale,  $V = 50 \text{ m s}^{-1}$ , the first baroclinic dry gravity wave speed; (c) the timescale,  $T = L/V = 8 \text{ h}$ ; (d) the temperature scale,  $\theta_{eb}^* = 10 \text{ K}$ ; (e) the mean convective updraft intensity scale in the RCE,  $W = (|Q_{R0}|H_m)/(\bar{\alpha}\sigma_c)$ , which varies with the RCE since  $\sigma_c W = \bar{m}_c$ , the mass flux at RCE; (f) the heating intensity scale,  $|Q_{R0}|$  of  $1 \text{ K day}^{-1}$ . The linearization procedure is fairly straightforward and yields the following equations:

$$\begin{aligned}
\frac{\partial u_1}{\partial t} &= \frac{\bar{\alpha}\theta_{eb}^*}{V^2} \frac{\partial \theta_1}{\partial x} - \frac{C_D^0 L}{h} \frac{1}{1+b} \left[ \frac{u_0^2 + 2\bar{u}^2}{(u_0^2 + \bar{u}^2)^{1/2}} u_1 - \frac{b\bar{u}^2}{(u_0^2 + \bar{u}^2)^{1/2}} u_2 \right] - \frac{T}{\tau_D} u_1, \\
\frac{\partial u_2}{\partial t} &= \frac{\bar{\alpha}\theta_{eb}^*}{V^2} \frac{\partial \theta_2}{\partial x} - \frac{C_D^0 L}{h} \frac{b}{1+b} \left[ \frac{\bar{u}^2}{(u_0^2 + \bar{u}^2)^{1/2}} u_1 + \frac{u_0^2 + (1-b)\bar{u}^2}{(u_0^2 + \bar{u}^2)^{1/2}} u_2 \right] - \frac{T}{\tau_D} u_2, \\
\frac{\partial \theta_1}{\partial t} &= \frac{T|Q_{R0}|}{\theta_{eb}^*} w_c + \frac{\bar{\alpha}}{\theta_{eb}^*} \frac{\partial u_1}{\partial x} - \frac{T}{\tau_R(1+s)} \theta_1, \quad \frac{\partial \theta_2}{\partial t} = \frac{T|Q_{R0}|}{\theta_{eb}^*} q_2 + \frac{\bar{\alpha}}{4\theta_{eb}^*} \frac{\partial u_2}{\partial x} - \frac{sT}{\tau_R(1+s)} \theta_2, \\
\frac{\partial \theta_{eb}}{\partial t} &= -\frac{C_\theta^0 L}{h} (u_0^2 + \bar{u}^2)^{1/2} \theta_{eb} + \frac{C_\theta^0 L}{h} (1 - \bar{\theta}_{eb}) \frac{\bar{u}}{(u_0^2 + \bar{u}^2)^{1/2}} u_1 - \frac{C_\theta^0 L}{h} (1 - \bar{\theta}_{eb}) \frac{b\bar{u}}{(u_0^2 + \bar{u}^2)^{1/2}} u_2 \\
&\quad - (\bar{\theta}_{eb} - \bar{\theta}_{em}) \left\{ \frac{TW\sigma_c}{h} (w_c - \alpha_2 q_2) + \frac{H_m}{h} \left( \frac{\partial u_1}{\partial x} - \frac{\alpha_2}{4} \frac{\partial u_2}{\partial x} \right) + \frac{TW\sigma_c}{h} \left( \frac{1-\Lambda}{\Lambda} \right) \left[ (1-\mu)w_c + \frac{\mu}{s} q_2 \right] \right\} \\
&\quad - \frac{TW\sigma_c}{h} \frac{1}{1+s} \left( \frac{1}{\Lambda} - \alpha_2 s \right) \theta_{eb}, \\
\frac{\partial q_2}{\partial t} &= \frac{T}{\tau_s} (s w_c - q_2), \quad w_c = (1+s) \frac{c_p \Gamma_m H}{W^2} \frac{\theta_{eb}^*}{\theta_0} (\theta_{eb} - \gamma \theta_1 + \gamma \alpha_2 \theta_2).
\end{aligned} \tag{3.1}$$

Recall from the discussion below equation (2.5) that the deep penetrative convection is modeled through two parameters, the area fraction  $\sigma_c$ , and the typical height  $H$ . Note that in the nondimensional units utilized here,  $(H/W^2)$  automatically contains the combination  $\sigma_c^2 H$ , which is scale invariant for any RCE with all other external parameters fixed in (2.17). Thus, the consequences of varying  $\sigma_c$  for linear theory at the RCE in (2.17) are completely equivalent to varying  $H$ . Also, note that the other coefficients in (3.1) involving  $\sigma_c$  without  $H$  exhibit no dependence on  $\sigma_c$  because they enter in the combination  $W\sigma_c$ .

### a. Basic waves and instabilities

The system in (3.1) involves six prognostic equations that correspond to six normal modes at each wave-number,  $k$ . In the following subsections, various properties of the normal modes with form,  $\mathbf{U} = \mathbf{C} \exp[i(kx - \omega(k)t) + d(k)t]$  will be discussed for the linear system in (3.1). The growth rates  $d(k)$  and the phase velocity,

$\omega(k)/k$ , of the normal modes as well as the structure of the eigenvectors will be discussed below. In the absence of a barotropic mean wind, east–west symmetry in (3.1) is preserved, so that each eastward mode has a symmetric westward analog and vice versa. It will suffice, therefore, to study standing waves and modes with only one direction of propagation, which we choose to be eastward below.

### 1) STRATIFORM MODES

It was established in section 2c that the updrafts  $\bar{w}_c$  at the radiative convective equilibrium depend strongly on the cumulus convection area fraction,  $\sigma_c$ . The stability properties of the linear system in (3.1) are also extremely sensitive to variations in  $\sigma_c$ . In particular, the strongest instability occurs at large values of  $\sigma_c$ , while weak or no instability is observed at small  $\sigma_c$  in the range,  $0.001 < \sigma_c < 0.01$ . Though stability properties change continuously as  $\sigma_c$  is varied, it is useful to consider three specific values of the cumulus convection

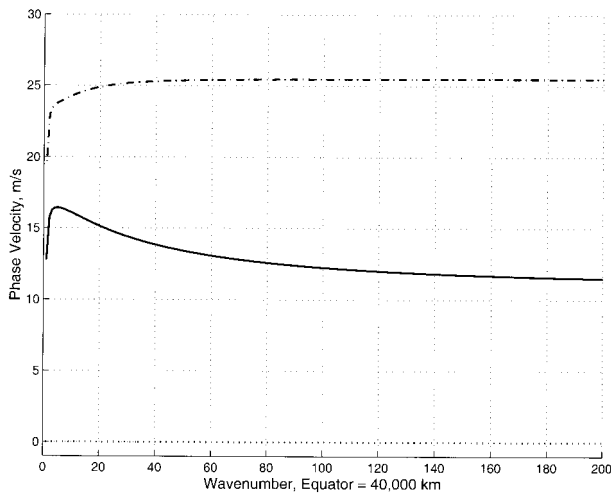


FIG. 1. Generalized phase velocity diagram for slow eastward (stratiform) waves (thick solid line), fast eastward waves (dash-dotted line), and stationary waves (dotted line) in the TVBM model.

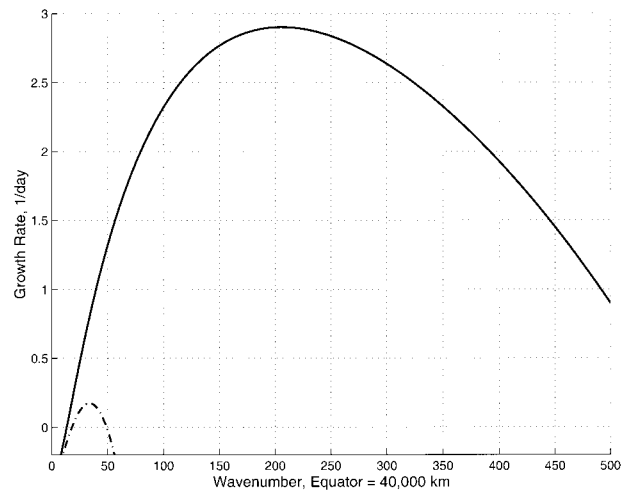


FIG. 2. Growth rates diagram for stratiform waves in the cluster (solid line) and scale-selective (dash-dotted line) regime.

area fraction,  $\sigma_c = 0.01, 0.0014, 0.001$ , to illustrate the three distinct regimes of instability.

Among these three values of  $\sigma_c$ , the strongest instability corresponds to  $\sigma_c = 0.01$ . The generalized phase velocity diagram for this case is presented in Fig. 1. The term “generalized phase velocity” is utilized in this paper to denote the ratio  $\omega(k)/k$ , where  $\omega(k)$  is the imaginary part of an eigenvalue and  $k$  is the wavenumber. This ratio reduces to the standard phase velocity for purely imaginary eigenvalues. The diagram in Fig. 1 represents normal modes of (3.1) with nonnegative generalized phase speeds. Among six normal modes there is a pair of slow ( $10\text{--}15\text{ m s}^{-1}$ ) waves, represented by a solid line; a pair of fast modes (approximately  $25\text{ m s}^{-1}$ ), represented by a dashed dotted-line; and two standing modes, both represented by a dotted line. Only the slow modes yield instability; their growth rates are shown in Fig. 2. The band of instability for the slow waves is fairly wide. It covers wavelengths ranging from  $L = 3000\text{ km}$  to  $L = 70\text{ km}$ , with the strongest instability of  $2.9\text{ day}^{-1}$  at  $L = 195\text{ km}$ . Since the peak of instability in this regime is located in the squall line cluster range of scales, it is logical to call it the cluster regime. Note that at the larger scales of order  $1000$  to  $2000\text{ km}$  where instability occurs, the phase velocity of these moist waves is close to the  $15\text{ m s}^{-1}$  phase velocity in the observational dataset from Wheeler and Kiladis (1999) and Wheeler et al. (2000).

The second regime of stratiform instability corresponds to  $\sigma_c = 0.0014$ . The growth rates diagram for this regime is represented by the dotted curve in Fig. 2. The band of unstable waves is much narrower in this regime; it covers only waves in the supercluster range, from  $L = 2200\text{ km}$  to  $L = 800\text{ km}$ . The largest growth rate of  $0.18\text{ day}^{-1}$  corresponds to the wavelength of  $1200\text{ km}$ . Since all variability in this regime is restricted to the supercluster range, it will be called the scale-selective or supercluster regime. The phase speed of the moist unstable waves is roughly  $15\text{ m s}^{-1}$ . The phase speed of  $15\text{ m s}^{-1}$  compares very favorably with those observed by Wheeler and Kiladis (1999) in their analysis of convectively coupled waves from outgoing long wave radiation (OLR) data. The spatial scale of  $1200\text{ km}$  in the lower troposphere for the unstable waves with the tilted structure shown below also roughly fits those titled structures observed by Wheeler et al. (2000). The main properties of stratiform waves in the scale-selective regime are shown in the second line of Table 2. Finally, the smallest value of the area fraction,  $\sigma_c = 0.001$ , generates the third regime, with no instability at all wavenumbers.

The last line in Table 2 shows the main properties of stratiform waves in this regime. The direct comparison of the cluster, scale-selective, and stable regimes in Table 2 shows that convective and short cluster scale stratiform waves reach stability at significantly larger values of the convection area fraction than waves in the su-

TABLE 2. Cluster ( $\sigma_c = 0.01$ ), scale-selective ( $\sigma_c = 0.0014$ ), and stable ( $\sigma_c = 0.001$ ) regimes of stratiform waves. From left to right: intensity of convective updrafts at RCE ( $w_c$ ), maximum growth rate ( $d_{\max}$ ), generalized phase and group velocities of the most unstable mode ( $c_{\max}, g_{\max}$ ), wavelength of the most unstable mode ( $L_{\max}$ ), longest and shortest wavelengths with instability ( $L_1, L_2$ ), and phase velocities at these wavelengths ( $c_1, c_2$ ).

$\sigma_c$	$\bar{w}_c, \text{ m s}^{-1}$	$d_{\max}, \text{ day}^{-1}$	$c_{\max}, \text{ m s}^{-1}$	$g_{\max}, \text{ m s}^{-1}$	$L_{\max}, \text{ km}$	$L_1, \text{ km}$	$c_1, \text{ m s}^{-1}$	$L_2, \text{ km}$	$c_2, \text{ m s}^{-1}$
0.01	0.30	2.9	11.5	10.8	195	3000	15.8	70	11
0.0014	2.1	0.18	14.4	12.3	1200	2200	15.6	800	13.6
0.001	3	-0.19	15.8	14	2000	N/A	N/A	N/A	N/A

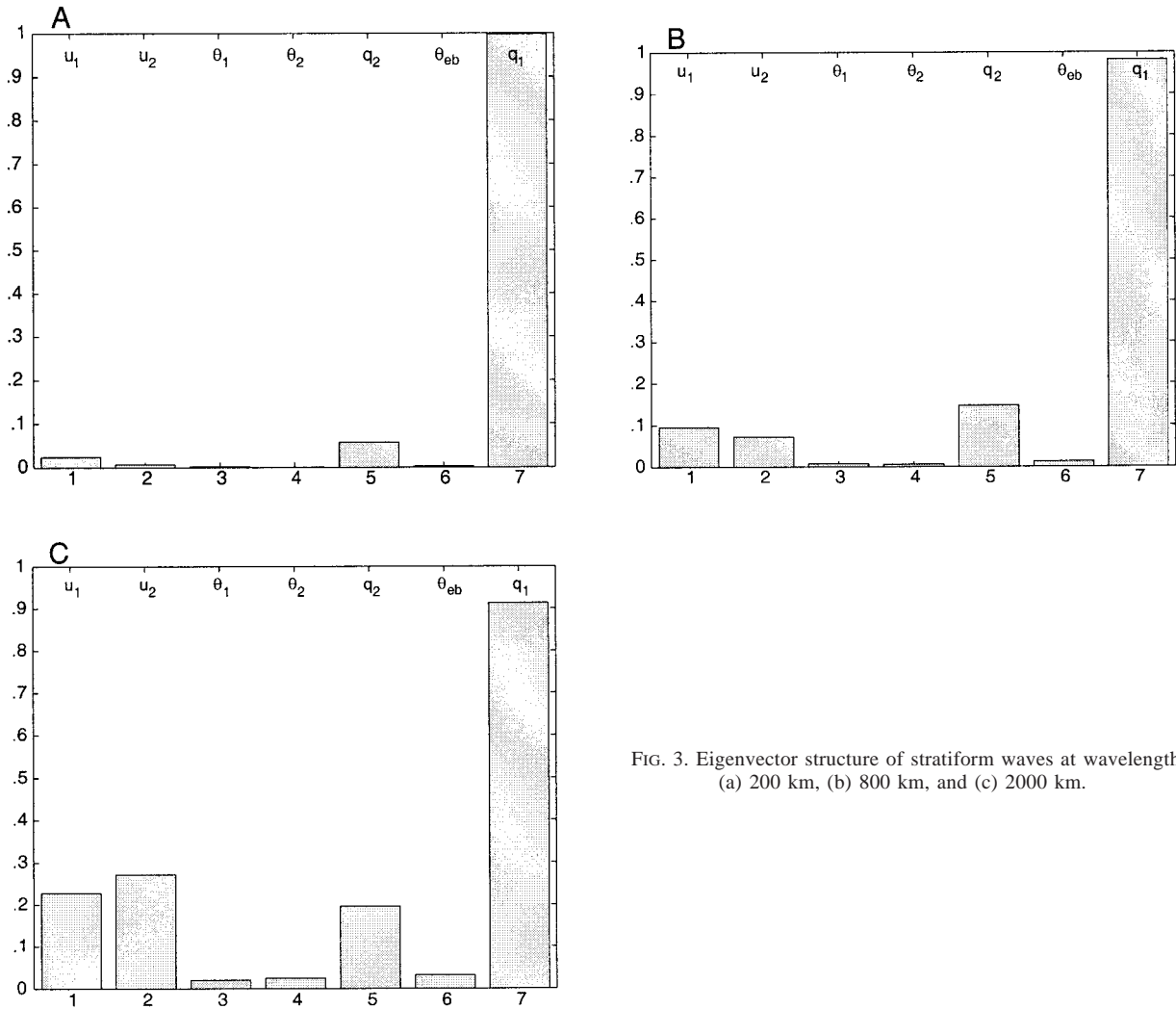


FIG. 3. Eigenvector structure of stratiform waves at wavelengths: (a) 200 km, (b) 800 km, and (c) 2000 km.

percluster range. Since the fastest unstable stratiform modes are typically located at the longwave end of the instability band (see Fig. 1), the generalized phase and group speeds of the most unstable wave increase from approximately  $11.5 \text{ m s}^{-1}$  and  $10.8 \text{ m s}^{-1}$  to approximately  $16 \text{ m s}^{-1}$  and  $14 \text{ m s}^{-1}$ , as  $\sigma_c$  decreases from 0.01 to 0.001. Remarkably, three similar regimes of instability were obtained by numerical simulations (Mapes 2000), where variability of the stratiform waves was controlled by the level of convective inhibition. Here we establish analytically that the area fraction of convective activity controls the structure of the instability in the simplified parameterization, in a similar fashion. See the parameter  $M$  and its effect on different regimes discussed in section 4 of Mapes (2000).

A useful description of the bulk properties of various eigenvectors is provided by the bar diagrams, such as depicted in Fig. 3 for the case  $\sigma_c = 0.01$ . The variables  $u_1, u_2, \theta_1, \theta_2, q_1, q_2,$  and  $\theta_{eb}$  are represented in a bar

diagram as follows: (a) each bar represents the magnitude of an underlying variable; (b) the height of each bar is scaled with respect to the corresponding scaling constant:  $V$ , for the velocity components,  $\theta_e^*$ , for the temperature components, and  $|Q_{R0}|$  for the heating components; (c) the sum of the squares of bar heights is normalized to one. Bar diagrams for the slow unstable eastward mode are presented in Fig. 3 for the following three length scales: a short cluster scale of 200 km, an intermediate scale of 800 km, and a supercluster scale of 2000 km. The second baroclinic (stratiform) components are significant in the structure of the slow modes at all three wavelengths. It is natural, therefore, to call these modes the stratiform waves. Observe that these stratiform waves in the absence of convective coupling reduce to the first baroclinic mode dry gravity waves, propagating with phase speeds of  $50 \text{ m s}^{-1}$ . Convective coupling slows these waves significantly, to approximately  $10\text{--}15 \text{ m s}^{-1}$ , as follows from Fig. 1. There are

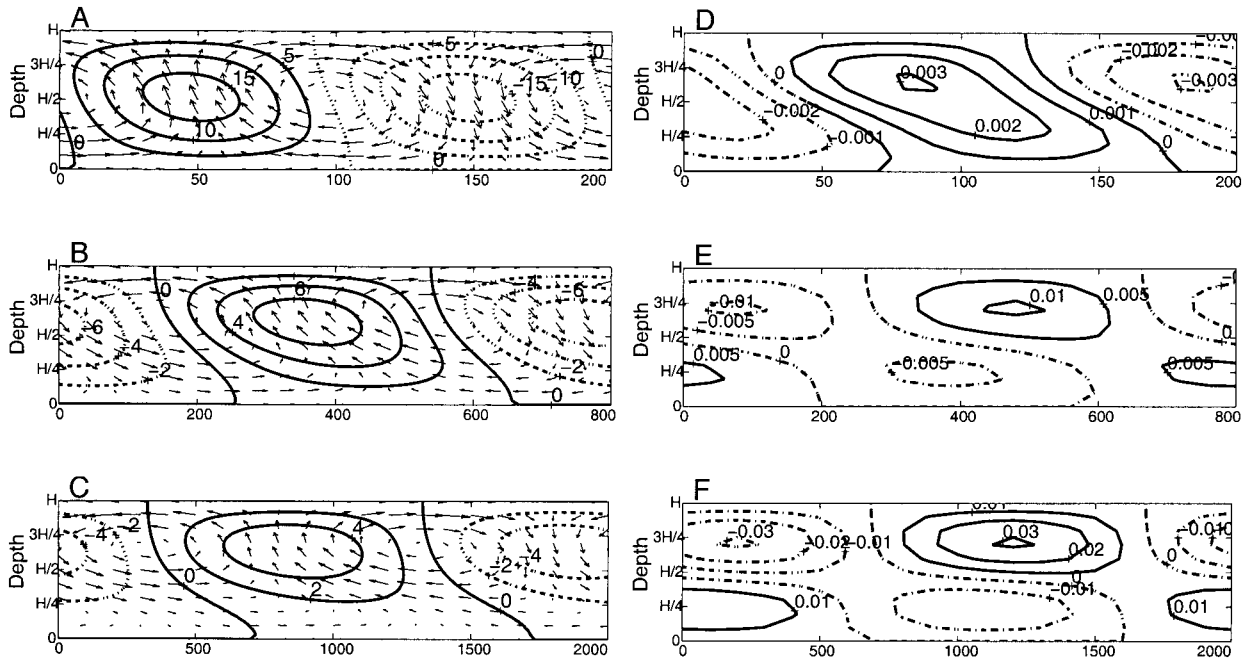


FIG. 4. Large-scale flow (arrows) and convective heating patterns (contour lines) for stratiform waves at wavelengths: (a) 200 km, (c) 800 km, (e) 2000 km. Positive (lined) and negative (dashed) potential temperature anomalies for stratiform waves at wavelengths: (b) 200 km, (d) 800 km, (f) 2000 km.

other waves associated with the second baroclinic mode propagating at  $25 \text{ m s}^{-1}$  and described below.

The large-scale flow, convective heating patterns, and temperature anomaly fields associated with stratiform waves are reconstructed from the appropriate eigenvectors according to (2.2) and are shown in Fig. 4 for  $L = 200, 800,$  and  $2000 \text{ km}$ . The analytic formulas utilized in the reconstruction process are presented in the appendix. Note that intensities of convective heating and potential temperature anomalies represent only relative quantities in the linear theory. The aspect ratio of the horizontal and vertical scales in each panel is adjusted with respect to the wavelength, keeping the vertical scale fixed. A typical vertical extent of the waves depicted in Fig. 4 is equal to approximately  $10 \text{ km}$ . Note that the temperature profile in the upper troposphere lags behind the profile in the lower troposphere providing a wave tilt qualitatively similar to those observed in Wheeler and Kiladis (1999). This wave tilt and its sensitivity to parameters is discussed below.

Figure 5 depicts the zonal distribution of CAPE for a stratiform wave with the wavelength of  $800 \text{ km}$ . Note

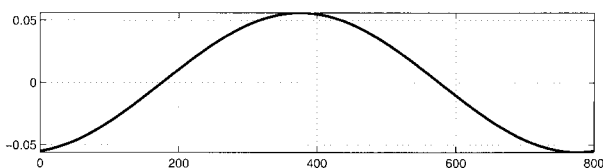


FIG. 5. Convective available potential energy for the eastward stratiform wave with the wavelength  $800 \text{ km}$ .

that positive CAPE anomalies in Fig. 5 are correlated with the regions of convective heating and are in phase with the ascending branch of the circulation anomaly in Fig. 4. The buildup of CAPE through the second baroclinic mode is discussed in section 4. A new feature of the stratiform waves, absent in the OVBM model, is the tilting of waves, clearly seen in Fig. 4. A more detailed discussion of the stratiform waves structure will be given in section 4 below. For the readers' convenience, all main stability and wave properties of eastward stratiform waves in the cluster regime are summarized in the first line of Table 2. The large-scale flow, convective heating patterns, and temperature anomaly field in the scale-selective regime are not displayed here for brevity, since they are qualitatively similar to the patterns presented in Fig. 4.

## 2) OTHER MODES

Fast eastward modes at the wavelengths,  $200, 800,$  and  $2000 \text{ km}$ , are illustrated by the bar diagrams in Fig. 6. It is easy to observe that the second baroclinic components of the large-scale zonal velocity and dry temperature,  $u_2$  and  $\theta_2$ , dominate the first baroclinic components,  $u_1$  and  $\theta_1$ . Also, according to Fig. 1, the generalized phase speed of these waves at all three wavenumbers above is equal to approximately  $25 \text{ m s}^{-1}$ , which coincides with the speed of dry gravity waves of the second baroclinic mode. The large-scale flow patterns for these waves, not depicted here, are also essentially equivalent to the double-cell flow patterns of

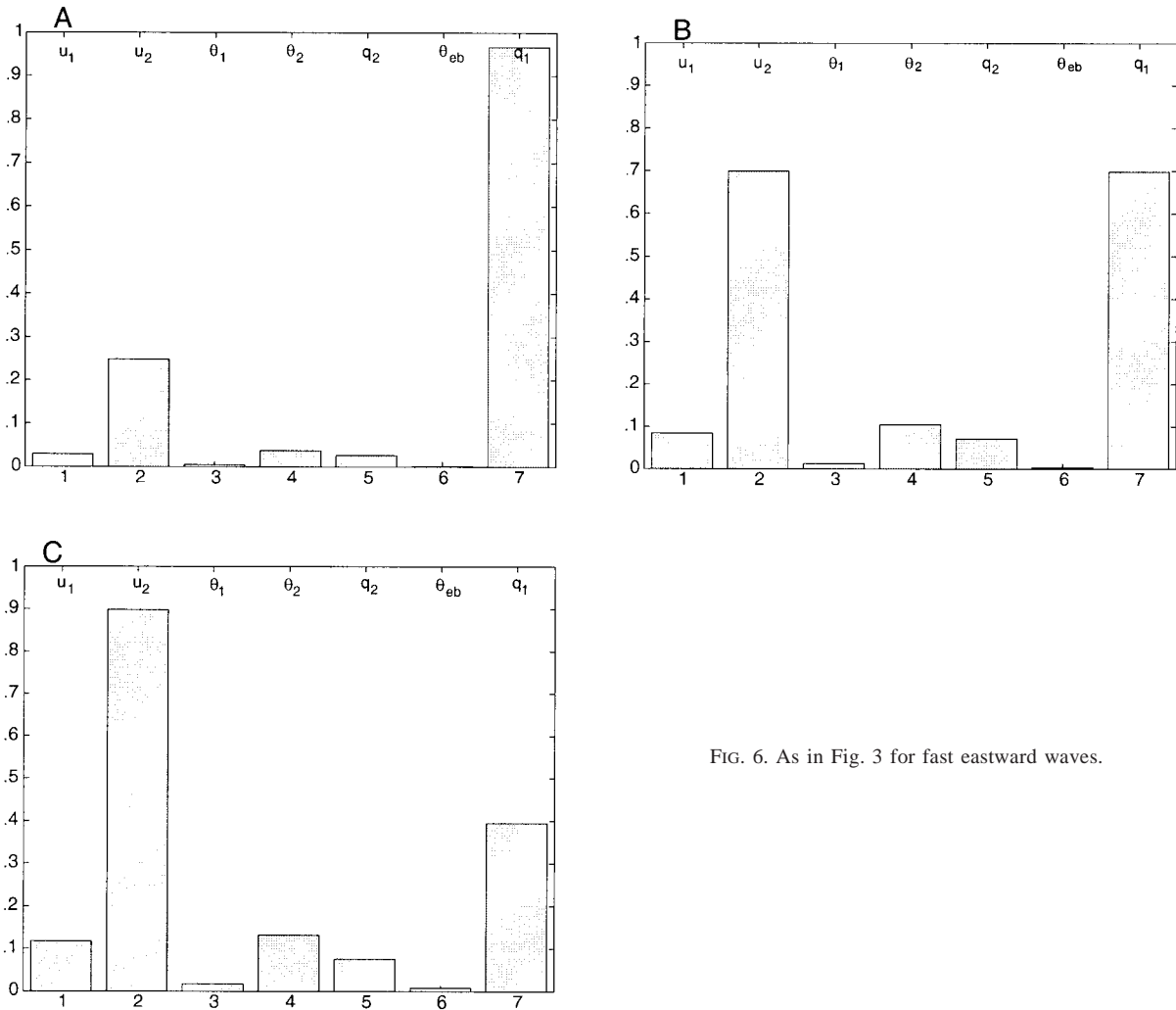


FIG. 6. As in Fig. 3 for fast eastward waves.

the second baroclinic mode dry gravity waves. Thus, the  $25 \text{ m s}^{-1}$  modes can be regarded as the moist analogs of the second baroclinic mode dry gravity waves. Note, however, that this analogy is incomplete: the  $25 \text{ m s}^{-1}$  waves of the TVBM model carry nontrivial moisture and convective activity, as illustrated by Fig. 6, and are also slightly damped, in contrast to the dry gravity waves.

Both remaining normal modes of the system in (3.1)

are stationary and are damped at all wavenumbers. One of these modes is entirely dominated by the vertical gusts of deep penetrative convection and is extremely strongly damped. This mode is associated with a rapid adjustment of CAPE perturbations to equilibrium and is a two-and-a-half layer analog of the CAPE adjustment mode arising in the OVBM model (Majda and Shefter 2000). The second stationary mode represents shallow convection in the TVBM model. The large-scale veloc-

TABLE 3. Sensitivity of stability and propagation properties of eastward stratiform waves to  $\mu$ . From left to right: maximum growth rate ( $d_{\max}$ ), generalized phase and group velocities of the most unstable mode ( $c_{\max}$ ,  $g_{\max}$ ), wavelength of the most unstable mode ( $L_{\max}$ ), longest and shortest wavelengths with instability ( $L_1$ ,  $L_2$ ).

$\mu$	$d_{\max}$ , $\text{day}^{-1}$	$c_{\max}$ , $\text{m s}^{-1}$	$g_{\max}$ , $\text{m s}^{-1}$	$L_{\max}$ , km	$L_1$ , km	$L_2$ , km
0.1	0.37	14.8	14.4	400	1600	180
0.3	1.3	13.3	12.7	290	2500	100
0.5	2.9	11.5	10.8	200	3000	70
0.7	6.1	9.3	8.3	120	3600	convective
0.9	15.0	6.2	4.9	60	4000	convective

TABLE 4. Sensitivity of stability and propagation properties of eastward stratiform waves to  $\Lambda$ . From left to right: maximum growth or minimum damping rate ( $d_{\max}$ ), generalized phase and group velocities of the most unstable or least damped mode ( $c_{\max}$ ,  $g_{\max}$ ), wavelength of the most unstable or least damped mode ( $L_{\max}$ ), longest and shortest wavelengths with instability ( $L_1$ ,  $L_2$ ).

$\Lambda$	$d_{\max}$ , day $^{-1}$	$c_{\max}$ , m s $^{-1}$	$g_{\max}$ , m s $^{-1}$	$L_{\max}$ , km	$L_1$ , km	$L_2$ , km
0.9	2.9	11.5	10.8	195	3000	70
0.95	2.5	8.2	7.5	175	2100	72
0.98	1.9	5.3	4.7	160	1300	75
0.99	1.3	3.9	3.4	155	870	80
0.995	0.76	2.9	2.4	155	580	90
0.998	0.086	2.0	1.7	175	270	135
1	-0.2	0	0	Largest	N/A	N/A

ity and convective heating patterns associated with this mode are organized in periodic cells located near the bottom of the domain and intensely communicate with the boundary layer, while the upper parts of the domain essentially remain at equilibrium.

### b. Sensitivity with parameter changes

Two important sensitivity parameters for the system in (3.1) are 1) the relative strength of the second baroclinic mode mass flux,  $\mu$ , and 2) the precipitation efficiency,  $\Lambda$ . Another interesting parameter to vary is the stratiform adjustment time,  $\tau_s$ . Tables 3 and 4 illustrate the behavior of the stratiform modes when either  $\mu$  or  $\Lambda$  are varied for the constant value  $\sigma_c = 0.01$ . All other parameters in these simulations have the fixed values given in Table 1. Observe that small values of  $\mu$  represent a weak influence of the second baroclinic component of convective downdrafts on the dynamics of  $\theta_{eb}$ . Table 3 displays main properties of the stratiform

TABLE 5. Sensitivity of stability and propagation properties of the eastward stratiform wave to the stratiform adjustment time  $\tau_s$  for various values of  $\mu$  for the benchmark value  $\Lambda = 0.9$  with  $\alpha_2 = 0.05$ .

$\mu/\tau_s$	15 min	3 h	6 h
0.2	$gr_{\max} = 3.8$ $L_{\max} = 75$ km $L_1 = 400$ km $L_2 = 40$ km $c = 14.6$ m s $^{-1}$	$gr_{\max} = 0.5$ $L_{\max} = 400$ km $L_1 = 1600$ km $L_2 = 160$ km $c = 15.5$ m s $^{-1}$	$gr_{\max} = 0.05$ $L_{\max} = 600$ km $L_1 = 800$ km $L_2 = 400$ km $c = 13.8$ m s $^{-1}$
0.4	$gr_{\max} = 11$ $L_{\max} = 50$ km $L_1 = 500$ km $L_2 = \text{convective}$ $c = 13.3$ m s $^{-1}$	$gr_{\max} = 1.7$ $L_{\max} = 250$ km $L_1 = 2000$ km $L_2 = 90$ km $c = 13.7$ m s $^{-1}$	$gr_{\max} = 0.7$ $L_{\max} = 400$ km $L_1 = 2000$ km $L_2 = 140$ km $c = 12.2$ m s $^{-1}$
0.6	Maximum growth at convective scales	$gr_{\max} = 4$ $L_{\max} = 160$ km $L_1 = 2500$ km $L_2 = \text{convective}$ $c = 11.5$ m s $^{-1}$	$gr_{\max} = 2$ $L_{\max} = 270$ km $L_1 = 2700$ km $L_2 = 90$ km $c = 10.2$ m s $^{-1}$
0.8	Maximum growth at convective scales	$gr_{\max} = 9$ $L_{\max} = 100$ km $L_1 = 4000$ km $L_2 = \text{convective}$ $c = 8.7$ m s $^{-1}$	$gr_{\max} = 5$ $L_{\max} = 130$ km $L_1 = 4000$ km $L_2 = 55$ km $c = 7.6$ m s $^{-1}$

waves for  $0.1 < \mu < 0.9$ . A strong second baroclinic component of convective downdrafts (large  $\mu$ ) tends to enhance the instability of stratiform waves, while small  $\mu$  produces a weaker instability. The short wavelength end of the instability band at large  $\mu$  belongs to the ‘‘convective’’ range, that is,  $L < 50$  km in this context. In the limiting case,  $\mu = 0$ , stratiform convective downdrafts are eliminated completely. Therefore, a more stable behavior of the stratiform waves at small  $\mu$  indicates the importance of stratiform convective downdrafts for the instability of stratiform waves. Finally, the generalized phase speed of the most strongly unstable mode decreases from 14.8 to 6.2 m s $^{-1}$  as  $\mu$  increases from 0.1 to 0.9 and the length scale of these waves decreases.

The effects of the second sensitivity parameter,  $\Lambda$ , on the stability properties are summarized in Table 4. The growth rates and the width of the instability band decrease rapidly as  $\Lambda$  increases from 0.9 to 1. The threshold value, near  $\Lambda = 0.998$ , separates stable and unstable regimes. The generalized phase speeds of the most unstable modes are also extremely sensitive to  $\Lambda$  and decrease from about 16 m s $^{-1}$  to zero as  $\Lambda$  increases from 0.9 to 1. It is important to emphasize that strong sensitivity to  $\mu$  and  $\Lambda$  extends only to the behavior of small perturbations near radiative convective equilibria, but not to the RCE values themselves, which change only slightly as  $\mu$  and  $\alpha_2$  vary.

It is also interesting to test the sensitivity to the stratiform adjustment time,  $\tau_s$ , in (2.9). All studies described in detail here use the value  $\tau_s = 3$  h suggested by Mapes (2000). The RCE is independent of  $\tau_s$ . Table 5 shows the sensitivity of the stability and wave properties of the eastward stratiform mode for three different adjustment times,  $\tau_s = 15$  min, 3 h, 6 h for a range of  $\mu$ ,  $\mu = 0, 0.2, 0.4, 0.6, 0.8$  for the RCE with  $\sigma_c = 0.01$  utilized throughout this paper. For a fixed  $\mu$ , the general trends are the following ones. When  $\tau_s$  is increased from 3 to 6 h, the band of instability moves to larger scales and the growth rates are diminished while the phase velocities decrease slightly. On the other hand, a very short adjustment time,  $\tau_s = 15$  min, leads to significantly larger growth rates than the benchmark case with maximum growth rates achieved at very small scales on the order of 50 km. Note that this means that the formal limit of the TVBM model reducing for  $\tau_s \rightarrow 0$  to the

OVBM model is in fact a singular perturbation limit with nonuniform behavior occurring at small wavelengths. While no details are given here, the structure of stratiform instability is remarkably insensitive to the value of  $\alpha_2$  used in (2.7) and (2.12); even the parameter value  $\alpha_2 = 0$  can have unstable waves for the typical benchmark parameter regime. Decreasing  $\alpha_2$  does increase instability as the reader can observe by comparing Table 3 with  $\alpha_2 = 0.1$  and the middle of Table 5 with  $\alpha_2 = 0.05$  for  $\tau_s = 3$  h.

#### 4. The dynamics of stratiform instability

It was shown in the previous section that stratiform modes of the two-and-a-half-layer model are typically unstable in the absence of barotropic mean flow. This property makes them very different from the moist gravity waves of the one-and-a-half-layer model with the same parameter values for RCE where all waves are stable without barotropic mean flow (Majda and Shefter 2000). In this section, the authors present a more detailed dynamic description of the stratiform mode structure. The life cycle of stratiform waves can be split naturally into two separate phases. In the first phase, deep convection, formed in the regions of large CAPE, triggers stratiform precipitation in the wake, and contributes to the formation of structures resembling trop-

ical squall lines. In the second phase, stratiform CAPE production reinitializes the instability. The authors argue that this mechanism of stratiform instability is fundamentally different from the WISHE mechanism of instability (Emanuel 1987; Yano and Emanuel 1991), which is the driving force of instability for the OVBM models and requires a nontrivial barotropic mean wind.

##### a. Dynamic equation for CAPE budget

Deep convection in unstable stratiform waves is statically linked to CAPE fluctuations, through the ICAPE convective parameterization in (2.8). It is important, therefore, to understand how CAPE changes in time at various stages of the wave evolution. A simple analytical framework for this analysis can be obtained by forming the equation for CAPE anomalies as a linear combination of the appropriate equations in (3.1),

$$\begin{aligned} \frac{\partial(\text{CAPE})}{\partial t} &\equiv \frac{\partial(\theta_{eb} - \gamma\theta_1 + \alpha_2\gamma\theta_2)}{\partial t} \\ &= -K_1\theta_{eb} + F_1 + F_2, \end{aligned} \quad (4.1)$$

where  $F_1$  and  $F_2$  denote the forcing components from the first and second baroclinic modes. Here, for simplicity, small effects of radiative damping are neglected in the equations for  $\theta_1$  and  $\theta_2$ . The contributions,  $F_1$  and  $F_2$ , to the CAPE forcing are given by

$$\begin{aligned} F_1 &= \frac{C_\theta^0 L}{h} (1 - \bar{\theta}_{eb}) \frac{\bar{u}}{(u_0^2 + \bar{u}^2)^{1/2}} u_1 - \gamma \frac{T|Q_{R0}|}{\theta_{eb}^*} w_c - \gamma \frac{\bar{\alpha}}{\theta_{eb}^*} \frac{\partial u_1}{\partial x} \\ &\quad - (\bar{\theta}_{eb} - \bar{\theta}_{em}) \left\{ \frac{TW\sigma_c}{h} w_c + \frac{H_m}{h} \frac{\partial u_1}{\partial x} + \frac{TW\sigma_c}{h} \left( \frac{1 - \Lambda}{\Lambda} \right) (1 - \mu) w_c \right\}, \\ F_2 &= -\frac{C_\theta^0 L}{h} (1 - \bar{\theta}_{eb}) \frac{b\bar{u}}{(u_0^2 + \bar{u}^2)^{1/2}} u_2 + \gamma\alpha_2 \frac{T|Q_{R0}|}{\theta_{eb}^*} q_2 + \gamma\alpha_2 \frac{\bar{\alpha}}{4\theta_{eb}^*} \frac{\partial u_2}{\partial x} \\ &\quad + (\bar{\theta}_{eb} - \bar{\theta}_{em}) \left\{ \frac{TW\sigma_c}{h} \alpha_2 q_2 + \frac{\alpha_2}{4} \frac{\partial u_2}{\partial x} - \frac{TW\sigma_c}{h} \left( \frac{1 - \Lambda}{\Lambda} \right) \frac{\mu}{s} q_2 \right\}, \end{aligned} \quad (4.2)$$

while

$$K_1 = \frac{C_\theta^0 L}{h} (\bar{u}^2 + u_0^2)^{1/2} + \frac{TW\sigma_c}{h} \frac{1}{1 + s} \left( \frac{1}{\Lambda} - \alpha_2 s \right).$$

##### b. Mechanism of stratiform instability

Since eastward and westward stratiform waves are perfectly symmetric in the absence of mean wind, it is sufficient to consider only eastward-propagating waves. The main qualitative features of stratiform waves are universal in a wide range of scales and for both cluster

and scale-selective regimes of instability. Therefore, the detailed wave analysis in this section will be limited to the eastward stratiform wave in the cluster regime, with the wavelength 800 km, depicted in Figs. 4c and 4d.

The life cycle of a stratiform wave can be naturally separated into two stages. The first stage is illustrated by Fig. 7. It is convenient to identify the beginning of this first stage with a maximum of CAPE located near  $x = 380$  km in Fig. 5. The maximum of CAPE is linked through the ICAPE parameterization in (2.8) to a strong first baroclinic convective heating anomaly located near  $x = 400$  km in Fig. 7. Note that the stratiform (second baroclinic) component of convective heating almost

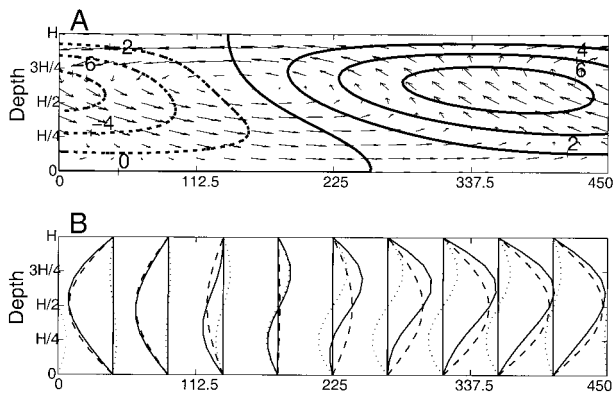


FIG. 7. Phase I of eastward stratiform wave life cycle, with wavelength 800 km: (a) large-scale velocity (arrows) and convective heating (contour lines) patterns, (b) convective heating rates (solid lines), decomposed into the first (dashed) and second (dotted) baroclinic components sampled at several locations.

vanishes near this location. The large-scale flow in this region is dominated by a strong vertical flow, driven by the gusts of penetrative convection. As the wave propagates eastward, deep convection triggers stratiform convection through the “delayed” stratiform adjustment mechanism expressed by (2.9). In Fig. 7, the region of deep convection is followed by a trailing stratiform wake, as indicated by the heating rate curve located near  $x = 180$  km. There, deep penetrative convection is switched off and the second baroclinic component of heating is positive and strong. Note that the large-scale flow in the stratiform wake is mainly horizontal, with a strong positive shear.

The entire wave fragment shown in Fig. 7 provides an adequate illustration for the stratiform waves at all scales of instability. In the cluster range, near the scale of the strongest instability,  $L = 200$  km, this fragment can be interpreted as a model for convective momentum transport in a tropical squall line (Moncrieff 1992; Emanuel 1994). Indeed, the structure depicted in Fig. 7 displays all the characteristic elements of a tropical squall line. A region of deep convection is accompanied by a strong ascending motion near  $x = 350$  km. This region is trailed by a stratiform wake with enhanced vertical shear. Observe also the descending return flow in the lower part of the domain extending from  $x = 0$  to  $x = 250$  km and an ascending front-to-rear flow that connects the deep convection region with the stratiform wake. Thus, the model parameterization with two baroclinic modes can capture features of convective momentum transport qualitatively including the enhanced vertical shear in the stratiform wake.

The second part of the stratiform wave life cycle is presented in Fig. 8. A strong downward motion develops at the back of the stratiform wake, near  $x = 775$  km. This flow is in phase with a cooling anomaly in the middle of the troposphere displayed in Fig. 4. The CAPE budget and its breakdown into the first and second baroclinic components, as described in Eq. (4.2), are shown

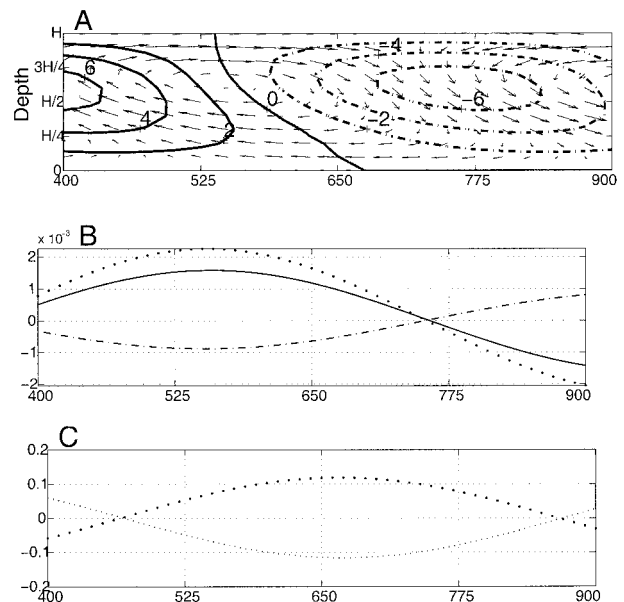


FIG. 8. Phase II of eastward stratiform wave life cycle, with wavelength 800 km: (a) large-scale velocity (arrows) and convective heating (contour lines) patterns; (b) total CAPE budget (solid line), total contribution to CAPE budget,  $F_1 + F_2$ , from first and second baroclinic modes (dotted line), contribution to CAPE budget from fluctuations in  $\theta_{eb}$  (dash-dotted line); (c) first (thin dotted line) and second (thick dotted line) baroclinic components of CAPE budget.

in Figs. 8b and 8c. From Fig. 8c it is easy to see that the contributions from the two baroclinic components,  $F_1$  and  $F_2$ , almost cancel each other, yielding the much smaller CAPE anomaly. The contribution of  $F_1 + F_2$  to the CAPE budget in (4.1) is compared with the overall CAPE budget in Fig. 8b. Note that this contribution is simultaneously in phase with the overall CAPE budget and also the forcing from the second baroclinic mode in Fig. 8c. The contribution from  $F_1 + F_2$  overshoots the magnitude of the total forcing in the CAPE budget by less than 15% in the region of maximum positive forcing associated with the tail of the stratiform wake. Thus, there is a much weaker contribution to the CAPE forcing of less than 15% arising from the negative contribution of  $-K_1\theta_{eb}$  from (4.1). In this sense, the increased CAPE production associated with the second baroclinic mode increases the CAPE to reinitialize the first phase of the instability discussed earlier in this section. Furthermore, the sensitivity of these features has been tested for several other weaker RCE either with unstable wavelengths at cluster and/or supercluster scales; the same conclusions as discussed above remain valid qualitatively for all of these regimes: the negative contributions from  $-K_1\theta_{eb}$  to the forcing of CAPE never exceeds 25% in the vicinity of maximum forcing coupled together with the simultaneous in-phase relation of positive forcing from the second baroclinic mode, and total forcing from  $F_1 + F_2$  in the CAPE budget equation.

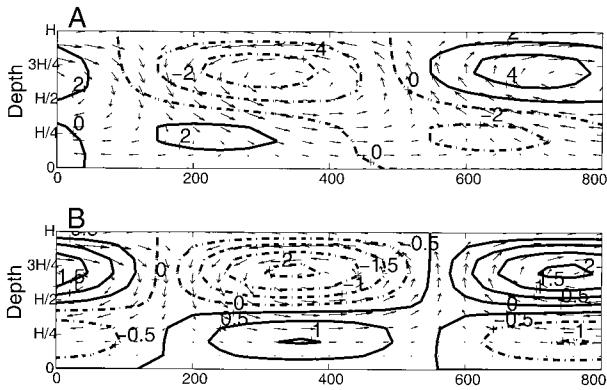


FIG. 9. Large-scale velocity (arrows) and potential temperature anomaly (contour lines) patterns for eastward stratiform wave with wavelength 800 km: (a) with  $\Lambda = 0.97$  and (b) with  $\Lambda = 1$ .

### c. Wave tilts and sensitivity to parameters

The tilting of large-scale flow, convective heating, and temperature anomaly patterns observed in Fig. 4 is a novel property of the stratiform waves. The tilts are present in a wide range of scales, with the eastward waves tilted upward toward the west, as depicted in Fig. 4, and the westward waves tilted in the opposite direction. According to Fig. 4, waves with the larger wavelengths have stronger tilts. A crude measurement of the tilt can be obtained by measuring the ratio of the horizontal and vertical extents of the zero contour curve in the heating diagrams or the temperature anomaly fields, such as in Fig. 4. This ratio is equal approximately to 1.5, 10, and 37 for the three wavelengths illustrated in Figs. 4a, 4c, and 4e. Similar wave tilts in the supercluster range were observed by Wheeler et al. (2000) through spectral reanalysis of OLR data for eastward-propagating equatorial Kelvin waves. Wheeler et al. (2000) discovered that temperature and velocity patterns had a “boomerang” shape in the vertical direction. The two halves of the boomerang were matched in the upper troposphere (150–200 mb), with the lower (troposphere) part tilted in the same way as the stratiform waves in Fig. 4, and the upper part tilted in the opposite direction. One can argue, therefore, that the wave tilts observed in the lower tropical troposphere are extremely robust and can be recovered in a simple model with only two modes in the vertical direction and explained through stratiform instability.

It was shown in section 3 that stability properties and propagation speeds of the stratiform modes are sensitive to the precipitation efficiency,  $\Lambda$ , and the relative strength of convective downdrafts,  $\mu$ . The wave tilts, however, have no sensitivity to the parameter  $\mu$  in the range  $0.1 < \mu < 0.9$ . At the same time, variations in  $\Lambda$  affect the tilts very strongly. As  $\Lambda$  increases, the tilts become less homogeneous in the vertical direction and weaker on average. Figure 9 shows the large-scale flow and temperature anomalies for the stratiform waves with  $\Lambda = 0.97$  and  $\Lambda = 1$ . The contours of temperature anomalies depicted in this figure represent only relative

strengths in the linear theory. The upper part of the wave structure shown in Fig. 9a ( $\Lambda = 0.97$ ) has a visibly weaker tilt than the lower part of this wave. The growth rate associated with this wave,  $0.52 \text{ day}^{-1}$ , is significantly weaker than the growth rate of  $1.32 \text{ day}^{-1}$  observed in the benchmark regime, with  $\Lambda = 0.9$ . Figure 9b illustrates the limiting case,  $\Lambda = 1$ , and reveals essentially no tilt. In this regime, convective downdrafts are completely switched off and the stratiform waves are damped at all wavenumbers.

## 5. Effects of barotropic mean on stratiform instability

In the TVBM model, instabilities of the stratiform waves are caused primarily by stratiform CAPE production and self-generated winds near the boundary layer. This mechanism is fundamentally different from the barotropic wind-generated WISHE mechanism, which is responsible for instabilities arising in the OVBM model and requires a nonzero mean flow. In this section, the effects of mean barotropic flow on stratiform instability in the TVBM models is assessed.

The character of stratiform instability in the absence of mean flow is controlled by  $\sigma_c$ . The value  $\sigma_c = 0.01$  sets the cluster regime, with a wide range of unstable waves and the strongest instability occurring on cluster scales of a few hundred kilometers. A smaller value,  $\sigma_c = 0.0014$ , establishes the scale-selective regime, with a narrow band of unstable modes and the peak of instability located in the supercluster range of approximately 1000 km.

A nontrivial mean wind,  $\bar{u} \neq 0$ , introduces an asymmetry between eastward and westward stratiform waves. Easterly mean winds are considered here since they naturally mimic the trade winds observed in the Pacific. Table 6 shows the main properties of eastward and westward stratiform waves stirred by easterly mean winds, ranging from zero to  $-10 \text{ m s}^{-1}$ , in the cluster regime with  $\sigma_c = 0.01$ . For each value of  $\bar{u}$ , this table shows the growth rate, wavelength, and the generalized phase velocity of the most unstable mode, the extent of the instability band, and the generalized phase speeds near the edges of the instability bubble. In contrast to the OVBM model, where external WISHE is the main source of instability in convectively coupled systems (Majda and Shefter 2001) and all waves are stable when  $\bar{u} = 0$ , WISHE plays only a secondary role in the TVBM model, splitting eastward and westward branches of already unstable stratiform waves.

Table 6a indicates that both the band of instability for eastward stratiform waves and the maximum growth rate increase for small values of the mean wind,  $0 < |\bar{u}| < 3 \text{ m s}^{-1}$ , which can be explained by the following observation. The easterly barotropic wind has the same direction as the local horizontal flow at the bottom of the troposphere arising in the reinitialization phase of the wave life cycle as discussed in section 4 and depicted in

TABLE 6. Influence of barotropic mean flow on instability of stratiform waves in the cluster regime,  $\sigma_c = 0.01$ . From left to right: maximum growth rate ( $d_{\max}$ ), generalized phase velocity of the most unstable mode ( $c_{\max}$ ), wavelength of the most unstable mode ( $L_{\max}$ ), longest and shortest wavelengths with instability ( $L_1, L_2$ ), and phase velocities at these wavelengths ( $c_1, c_2$ ).

$\bar{u}$ , m s <sup>-1</sup>	$d_{\max}$ , day <sup>-1</sup>	$c_{\max}$ , m s <sup>-1</sup>	$L_{\max}$ , km	$L_1$ , km	$c_1$ , m s <sup>-1</sup>	$L_2$ , km	$c_2$ , m s <sup>-1</sup>
Eastward modes							
0	2.9	11.5	195	3000	15.8	70	11
-1	3.1	11.5	190	3000	16.3	68	11.1
-2	3.2	11.5	185	3000	16.7	67	11.1
-3	3.3	11.5	185	2850	16.8	66	11.1
-5	3.2	11.5	185	2500	16.4	67	11.1
-7	3.0	11.5	190	2200	15.9	68	11.1
-10	2.7	11.5	190	1900	15.2	72	11.1
Westward modes							
0	2.9	-11.5	195	3000	-15.8	70	-11
-1	2.7	-11.5	200	3000	-15.3	73	-11.1
-2	2.5	-11.5	205	2850	-14.8	75	-11.1
-3	2.3	-11.4	207	2700	-14.5	78	-11.1
-5	2.1	-11.4	210	2500	-14.1	80	-11.1
-7	2.0	-11.4	210	2100	-13.9	83	-11.1
-10	1.8	-11.4	215	1700	-13.7	86	-11.1

Fig. 8. Therefore,  $\bar{u}$  enhances the effects of the local flow and enhances the instability through WISHE. At larger values of  $|\bar{u}|$ , increased frictional drag exerted by an external wind on the boundary layer overcomes the stirring effect and leads to a decrease of the growth rates and the instability band. The wavelength of the most unstable eastward wave remains constant for  $0 < |\bar{u}| < 10$  m s<sup>-1</sup> and equal to approximately 190 km. It must be noted that the strength of WISHE damping in this regime is sufficient only to split the eastward and westward branches, but not to damp the instability completely, at least in the physically meaningful range of  $\bar{u}$ .

Table 6b indicates that instability of the westward stratiform waves is diminished by the barotropic mean flow. Here, an easterly barotropic wind opposes local westerly winds arising in the lower troposphere during the reinitialization phase of the stratiform wave life cycle and damps the instability. The decrease of instability is accompanied by a weak drift of the instability peak from about 195 km to about 215 km. The comparison

of the stability properties for eastward and westward stratiform waves shows that eastward modes are always slightly more unstable than westward modes and the peak of instability for eastward modes corresponds to slightly shorter scales than the peak of instability for westward modes.

The fastest unstable eastward waves propagate with a generalized phase speed  $c_1 \approx 16$  m s<sup>-1</sup>, which is slightly faster than generalized phase speeds of the fastest westward waves. The fastest phase speed of 16 m s<sup>-1</sup> is close to the propagation speed of moist Kelvin waves, measured by Wheeler and Kiladis (1999) and also arises in the supercluster range. The generalized phase speed at the convective scale end of the spectrum is equal to approximately 11 m s<sup>-1</sup> for both eastward and westward stratiform waves. Finally, the stratiform wave structure is not affected by barotropic winds in this regime, and, in particular, the wave tilts do not change.

The scale-selective regime of instability corresponds to  $\sigma_c = 0.0014$  and is illustrated by Table 7, which

TABLE 7. Influence of barotropic mean flow on instability of stratiform waves in the scale-selective regime,  $\sigma_c = 0.0014$ . From left to right: maximum growth rate ( $d_{\max}$ ), generalized phase velocity of the most unstable mode ( $c_{\max}$ ), wavelength of the most unstable mode ( $L_{\max}$ ), longest and shortest wavelengths with instability ( $L_1, L_2$ ).

$\bar{u}$ , m s <sup>-1</sup>	$d_{\max}$ , day <sup>-1</sup>	$c_{\max}$ , m s <sup>-1</sup>	$L_{\max}$ , km	$L_1$ , km	$L_2$ , km
Eastward modes					
0	0.18	14.4	1200	2200	815
-1	0.23	14.6	1150	2200	770
-2	0.25	14.7	1100	2200	740
-3	0.25	14.7	1100	2200	740
-4	0.22	14.7	1100	1900	750
-6	0.12	14.8	1100	1650	830
-8	0	14.7	1100	N/A	N/A
Westward modes					
0	0.18	-14.4	1200	2200	815
-1	0.11	-14.3	1250	2200	900
-2	0.053	-14.2	1350	2000	1000
-3	0	-14.1	1400	N/A	N/A

displays the main properties of eastward and westward branches of stratiform waves for various values of  $\bar{u}$ . Since the extent of instability is small in this regime, the generalized phase speed is reported at the peak of instability only. It is easy to observe that qualitative trends in the scale-selective and cluster regimes are very similar. The instability of eastward modes is first enhanced by weak easterly winds, but then is diminished by WISHE friction for the stronger winds and is completely damped for  $|\bar{u}| > 8 \text{ m s}^{-1}$ . The effect of mean winds on the westward waves is more dramatic. In particular, a weak mean wind,  $\bar{u} = -3 \text{ m s}^{-1}$ , is sufficient to damp the instability completely. The most unstable eastward modes are slightly shorter than the most unstable westward modes, similarly to the cluster regime. Since the instability is localized in the supercluster range of scales, the most unstable modes in the scale-selective regime have faster generalized phase speeds than the most unstable modes in the cluster regime.

In conclusion, it is shown that the external barotropic mean wind in the two-and-a-half layer model plays only a secondary role in setting instability of the stratiform waves. Mean flow breaks the symmetry between the eastward and westward stratiform wave. The mean flow effects are stronger in the scale-selective regime, where westward modes can be stabilized by a weak mean wind.

## 6. Concluding discussion

A two-and-a-half layer intermediate model with two baroclinic modes of vertical resolution (TVBM) has been introduced in section 2 for analyzing and parameterizing convectively coupled waves. This model has the attractive feature that in a suitable limit of vanishing stratiform adjustment time and with the stratiform mode suppressed, a one-and-a-half-layer model parameterizing convectively coupled waves arises involving instantaneous CAPE adjustment (Majda and Shefter 2000).

A key parameter utilized in the theory is the area fraction for deep convection,  $\sigma_c$ . This area fraction depends significantly on the cooling rate at RCE and is estimated to be 0.001 to 0.002 for the cooling rate of  $1 \text{ K day}^{-1}$  utilized in this paper (see Fig. 7 of Robe and Emanuel 1996).

In section 3 it was established that as the area fraction of deep convection,  $\sigma_c$ , increases from  $\sigma_c = 0.001$  to  $\sigma_c = 0.0014$ , the parameterization passes from a stable regime of Moist Convective Damping (MCD) to a regime of unstable convectively coupled waves on supercluster scales with three key features of the waves observed by Wheeler and Kiladis (1999) and Wheeler et al. (2000): a phase velocity of roughly  $15 \text{ m s}^{-1}$ , a band of wavelengths in the troposphere ranging from  $O(1000)$  to  $O(2000)$  km, and "wave tilt" where the upper-troposphere temperature anomaly lags behind the lower-troposphere anomaly. An interesting future research direction is the development of a weakly nonlinear theory of convectively coupled waves in this re-

gime and the authors plan to pursue this in the near future. Another important fact from section 3 is that as  $\sigma_c$  increases further to  $\sigma_c = 0.01$ , the instability becomes broad band with the strongest growth rates on mesoscales with a similar spatial structure as occurs on larger scales. Obviously an important future problem is to include the effect of rotation in the results presented here in order to explain other convectively coupled equatorial waves in the observational record (Wheeler and Kiladis 1999; Wheeler et al. 2000); one appealing way to do this that the authors plan to pursue is through a simplified meridional low-order Galerkin truncation procedure (Majda and Shefter 2000). This analysis including rotation for ICAPE adjustment parameterization in one-and-a-half-layer models with a WISHE mechanism automatically reproduces a slow phase speed moist equatorial wave diagram with features resembling those in Wheeler and Kiladis (1999) (see Fig. 5 of Majda and Shefter 2000). Thus, we anticipate that when the effects of rotation are combined with the stratiform parameterization in the present paper, a more complete picture will emerge of all the convectively coupled equatorial waves in Wheeler and Kiladis (1999) including their vertical structure and phase velocities. Another appealing research direction is to develop extensions of these models into the stratosphere with the tropopause as a free surface (Yano and Emanuel 1991).

The dynamic mechanism for stratiform instability was studied quantitatively in section 4. In the first stage of the instability process, the stratiform model parameterization has a transparent analog of organized squall line clusters including enhanced vertical shear in the stratiform wake; the use of these models for studying upscale convective momentum transport certainly merits further investigation. Also, further study is warranted for the fashion in which the contributions to CAPE production from the second baroclinic mode reinitialize the convection in more realistic nonlinear models.

Finally, no barotropic mean winds are needed to generate stratiform instability and it was established in section 5 that such WISHE-induced instabilities have a secondary effect as compared with stratiform instability in these models. It is an interesting open question to understand the validity in the actual atmosphere of the stratiform instability picture versus the moist convective damping/WISHE instability picture (Emanuel et al. 1994) for explaining convectively coupled equatorial waves.

*Acknowledgments.* Matt Wheeler, George Kiladis, and Brian Mapes all presented excellent lectures on their work at the Atmosphere–Ocean seminar at the Courant Institute, which inspired this research. Andrew Majda is partially supported by Grants NSF DMS-9625795 and DMS-9972865, ONR N00014-96-1-0043, and ARO DAAG55-98-1-0129. Michael Shefter is supported as a postdoctoral fellow at the Courant Institute through ONR N00014-96-1-0043, ARO DAAG55-98-1-0129, and NSF DMS-9625795 and DMS-9972865.

## APPENDIX

## REFERENCES

### Analytic Formulas for Velocity, Temperature, and Convective Heating Fields for Linear Stratiform Waves

Linearized stability analysis for the system in (3.1) yields both eigenvalues and eigenvectors. The eigenvalues are utilized to compute the growth rates and generalized phase and group velocities of various modes by separating the real and imaginary parts. The spatial structure of waves corresponding to the normal modes of (3.1) can be reconstructed from the eigenvectors. For each wavenumber  $k$ , an eigenvector contains the (complex-valued) first and second baroclinic components  $u_1$ ,  $u_2$  of zonal large-scale velocity, the two baroclinic components,  $\theta_1$  and  $\theta_2$ , of potential temperature, the intensity of stratiform heating  $q_2$ , and also  $\theta_{eb}$ .

Large-scale velocity fields can be reconstructed from the eigenvector components in an agreement with (2.1), (2.2), and (2.3),

$$\begin{aligned}
 u(x, z) &= [\operatorname{Re}(u_1) \cos(kl_1x) - \operatorname{Im}(u_1) \sin(kl_1x)] \cos(l_2z) \\
 &\quad - [\operatorname{Re}(u_2) \cos(kl_1x) \\
 &\quad - \operatorname{Im}(u_2) \sin(kl_1x)] \cos(2l_2z), \\
 w(x, z) &= l_2[\operatorname{Re}(u_1) \sin(kl_1x) \\
 &\quad + \operatorname{Im}(u_1) \cos(kl_1x)] \sin(l_2z) \\
 &\quad - \frac{1}{2}l_2[\operatorname{Re}(u_2) \sin(kl_1x) \\
 &\quad + \operatorname{Im}(u_2) \cos(kl_1x)] \sin(2l_2z), \quad (\text{A.1})
 \end{aligned}$$

where  $l_1 = 2\pi R/L$ ,  $l_2 = 2\pi R/H$ , with the Rossby deformation radius,  $R = 1500$  km, the troposphere thickness,  $H = 8000$  m, and the earth's circumference,  $L = 40\,000$  km.

Similarly, potential temperature field and heating rates distribution can be extracted from the components  $\theta_1$ ,  $\theta_2$ , and  $\theta_{eb}$  according to (2.2), (2.3), (2.6), and (2.8),

$$\begin{aligned}
 \theta(x, z) &= [\operatorname{Re}(\theta_1) \cos(kl_1x) - \operatorname{Im}(\theta_1) \sin(kl_1x)] \sin(l_2z) \\
 &\quad - 2l_2[\operatorname{Re}(\theta_2) \cos(kl_1x) - \operatorname{Im}(\theta_2) \sin(kl_1x)] \sin(2l_2z), \\
 \text{Heating}(x, z) &= [\operatorname{Re}(q_1) \cos(kl_1x) - \operatorname{Im}(q_1) \sin(kl_1x)] \sin(l_2z) \\
 &\quad - 2l_2[\operatorname{Re}(q_2) \cos(kl_1x) \\
 &\quad - \operatorname{Im}(q_2) \sin(kl_1x)] \sin(2l_2z). \quad (\text{A.2})
 \end{aligned}$$

- Emanuel, K. A., 1987: An air-sea interaction model of intraseasonal oscillations in the Tropics. *J. Atmos. Sci.*, **44**, 2324–2340.
- , 1994: *Atmospheric Convection*. Oxford Press, 592 pp.
- , J. D. Neelin, and C. S. Bretherton, 1994: On large-scale circulations in convecting atmosphere. *Quart. J. Roy. Meteor. Soc.*, **120**, 1111–1143.
- Gill, A. E., 1982: *Atmosphere–Ocean Dynamics*. Academic Press, 666 pp.
- Houze, R. A., 1997: Stratiform precipitation in regions of convection: A meteorological paradox? *Bull. Amer. Meteor. Soc.*, **78**, 2179–2196.
- Kuo, H. L., 1974: Further studies of the influence of cumulus convection on large-scale flow. *J. Atmos. Sci.*, **31**, 1232–1240.
- Lindzen, R. S., 1974: Wave-CISK in the Tropics. *J. Atmos. Sci.*, **31**, 126–179.
- Majda, A. J., and M. G. Shefter, 2001: Waves and instabilities for model tropical convective parameterizations. *J. Atmos. Sci.*, **58**, 896–914.
- Mapes, B. E., 2000: Convective inhibition, subgridscale triggering energy, and “stratiform instability” in a toy tropical wave model. *J. Atmos. Sci.*, **57**, 1515–1535.
- , and R. A. Houze, 1995: Diabatic divergence profiles in western Pacific mesoscale convective systems. *J. Atmos. Sci.*, **52**, 1807–1828.
- Matsuno, T., 1966: Quasi-geostrophic motions in the equatorial area. *J. Meteor. Soc. Japan*, **44**, 25–43.
- Moncrieff, M. W., 1992: Organized convective systems: Archetypal dynamical models, mass and momentum flux theory, and parameterization. *Quart. J. Roy. Meteor. Soc.*, **118**, 819–850.
- , and E. Klinker, 1997: Organized convective systems in the tropical western Pacific as a process in general circulation models: A TOGA-COARE case study. *Quart. J. Roy. Meteor. Soc.*, **123**, 805–827.
- Neelin, J. D., and J. Yu, 1994: Modes of tropical variability under convective adjustment and the Madden–Julian oscillation. Part I: Analytical theory. *J. Atmos. Sci.*, **51**, 1876–1894.
- , and N. Zeng, 2000: A quasi-equilibrium tropical circulation model—Formulation. *J. Atmos. Sci.*, **57**, 1741–1766.
- Pedlosky, J., 1979: *Geophysical Fluid Dynamics*. Springer-Verlag, 624 pp.
- Robe, F. R., and K. A. Emanuel, 1996: Moist convective scaling: Some inferences from three-dimensional cloud ensemble simulations. *J. Atmos. Sci.*, **53**, 3265–3275.
- Wheeler, M., and G. N. Kiladis, 1999: Convectively coupled equatorial waves: Analysis of clouds and temperature in the wave-number-frequency domain. *J. Atmos. Sci.*, **56**, 374–399.
- , —, and P. Webster, 2000: Large-scale dynamical fields associated with convectively coupled equatorial waves. *J. Atmos. Sci.*, **57**, 613–640.
- Yano, J.-I., and K. A. Emanuel, 1991: An improved model of the equatorial troposphere and its coupling to the stratosphere. *J. Atmos. Sci.*, **48**, 377–389.
- , J. C. McWilliams, M. W. Moncrieff, and K. A. Emanuel, 1995: Hierarchical tropical cloud systems in an analog shallow-water model. *J. Atmos. Sci.*, **52**, 1723–1742.
- , M. W. Moncrieff, and J. C. McWilliams, 1998: Linear stability and single-column analyses of several cumulus parameterization categories in a shallow-water model. *Quart. J. Roy. Meteor. Soc.*, **124**, 983–1005.